TCAB1 prevents nucleolar accumulation of the telomerase RNA to promote telomerase assembly

Basma M. Klump [1,2,3], Gloria I. Perez [1], Eric M. Patrick[1,7], Kate Adams-Boone [1], Scott B. Cohen [4], Li Han [5], Kefei Yu [5], Jens C. Schmidt [1,6,*]

[1] Institute for Quantitative Health Sciences and Engineering, Michigan State University, East Lansing, MI, U.S.A.

[2] College of Osteopathic Medicine, Michigan State University, East Lansing, MI, U.S.A.

[3] Cellular and Molecular Biology Graduate Program, College of Natural Sciences, Michigan State University, East Lansing, MI, U.S.A.

[4] Children's Medical Research Institute and University of Sydney, Westmead, NSW 2145, Australia.

[5] Department of Microbiology and Molecular Genetics, Michigan State University, East Lansing, MI, U.S.A.

[6] Department of Obstetrics, Gynecology, and Reproductive Biology, Michigan State University, East Lansing, MI, U.S.A.

[7] Current address: Max Planck Institute of Immunobiology and Epigenetics, 79108, Freiburg im Breisgau, Germany.

[*] Correspondence: schmi706@msu.edu

Abstract

Localization of a wide variety of RNAs to non-membrane bound cellular compartments such as nucleoli, Cajal bodies, and stress-granules is critical for their function and stability. The molecular mechanisms that underly the recruitment and exclusion of specific RNAs from these phase-separated organelles is incompletely understood. Telomerase is a ribonucleoprotein (RNP) that is composed of the reverse transcriptase protein TERT, the telomerase RNA (TR), and several auxiliary proteins that associate with TR, including TCAB1. Here we show that in the absence of TCAB1, TR is tightly bound to the nucleolus, while TERT localizes to the nucleoplasm and is largely excluded from the nucleolus, significantly reducing telomerase assembly. Thus, nuclear compartmentalization by the non-membrane bound nucleolus counteracts telomerase assembly and TCAB1 is required to exclude the telomerase RNA from the nucleolus. Our work provides insight into the mechanism and functional consequences of RNA recruitment to organelles formed by phase separation proposes a new model explaining the critical role of TCAB1 in telomerase function.

38 **Introduction**

39 Human cells contain a number of non-membrane bound organelles that carry out critical
40 cellular functions. For instance, nucleoli and Cajal bodies are phase-separated nuclear
41 organelles that play important roles in the biogenesis and maturation of many cellular
42 RNAs (Hyman et al., 2014; Mitrea and Kriwacki, 2016). Nucleoli and Cajal bodies contain
43 a wide range of small nucleolar and small Cajal body-specific RNAs (snoRNAs and
44 scaRNAs, respectively). A subset of these snoRNAs and scaRNAs are bound by the
45 H/ACA complex, which contains NOP10, NHP2, GAR1, and the pseudouridylase
46 dyskerin, which modifies ribosomal and spliceosomal RNA precursors and other RNAs
47 (Angrisani et al., 2014). A key difference between snoRNAs and scaRNAs is the presence
48 of the Cajal-body box (CAB-box) motif in scaRNAs that directly associates with the
49 telomerase Cajal body protein 1 (TCAB1, also known as WRAP53) (Jády et al., 2004;
50 Schmidt and Cech, 2015; Venteicher et al., 2009). TCAB1 is required for the recruitment
51 of scaRNAs to Cajal bodies and in its the absence scaRNAs localize to the nucleolus
52 (Tycowski et al., 2009). Therefore, TCAB1 controls which phase-separated nuclear
53 organelle scaRNAs associate with. Importantly, the molecular mechanism by which
54 TCAB1 drives exclusion of scaRNAs from the nucleolus and facilitates their recruitment
55 to Cajal bodies is unknown. In addition, it is unclear whether miss-localization of scaRNAs
56 to the nucleolus has functional consequences.

57 The telomerase RNA (TR) is a scaRNA and, like other scaRNAs, its association
58 with nucleoli and Cajal bodies is controlled by TCAB1 (Schmidt and Cech, 2015).
59 Telomere maintenance by telomerase is essential for continuous proliferation of stem cell
60 populations in the human body, and most cancers require telomerase activity for their

survival (Stewart and Weinberg, 2006). To compensate for the incomplete replication of chromosome ends, telomerase appends TTAGGG repeats to the telomeric single-stranded overhang (Schmidt and Cech, 2015). Telomerase-mediated telomere maintenance requires three critical steps: telomerase assembly, telomerase recruitment to telomeres, and telomeric repeat synthesis (Schmidt and Cech, 2015). Mutations in several genes have been identified that cause deficiencies in one of these critical steps and lead to a variety of diseases known as telomere syndromes, which are characterized by premature depletion of stem cell populations (Armanios and Blackburn, 2012). In addition, telomerase is inappropriately activated in >85% of cancers (Stewart and Weinberg, 2006). While telomerase recruitment to telomeres (Nandakumar and Cech, 2013) and telomerase catalysis (Wu et al., 2017) have been studied extensively, much less is known about telomerase assembly. Importantly, telomerase assembly could be targeted to reduce telomerase activity in cancer cells, or to increase telomerase function in patients affected by genetically defined telomerase deficiency syndromes (Nagpal et al., 2020; Shukla et al., 2020).

Telomerase is a complex ribonucleoprotein (RNP). The core components of telomerase are the telomerase reverse transcriptase (TERT) protein, TR, the H/ACA complex, and TCAB1 (Schmidt and Cech, 2015). The primary function of the H/ACA complex is to stabilize TR, by directly binding to its 3'-end, preventing the exonucleolytic degradation of TR (Stuart et al., 2015; Tummala et al., 2015). The 3'-end formation of TR is tightly regulated by the competing activities of the poly-(A) polymerase PAPD5 and the nuclease PARN (Shukla et al., 2016; Tseng et al., 2015). Loss of TCAB1 function leads to telomere attrition in a variety of cell lines (Chen et al., 2018; Venteicher et al., 2009;

84 Vogan et al., 2016; Zhong et al., 2011). In addition, multiple mutations in TCAB1 have
85 been identified that cause misfolding of TCAB1 and lead to dyskeratosis congenita, a
86 telomere syndrome (Freund et al., 2014; Zhong et al., 2011). While these observations
87 highlight that TCAB1 is necessary for telomere synthesis, the underlying molecular
88 mechanism is unclear. Initially, it was proposed that TCAB1 is required for telomerase
89 recruitment to telomeres (Stern et al., 2012; Venteicher et al., 2009). A more recent study
90 suggested that TCAB1 is required for the correct folding of TR, and that its absence
91 causes a reduction in telomerase activity (Chen et al., 2018). All previous studies claim
92 that TCAB1 does not mediate telomerase assembly, a critical step in telomere
93 maintenance.

94 Here, we analyze telomerase assembly in intact cells and by purification of the
95 telomerase RNP and demonstrate that, contrary to previous findings, TCAB1 promotes
96 telomerase assembly *in vivo.* In the absence of TCAB1, TR is tightly associated with the
97 nucleolus while TERT is largely excluded from the nucleolus. This spatial separation of
98 TERT and TR, in the absence of TCAB1, is incompatible with proper telomerase
99 assembly. Furthermore, we show that the limited amount of telomerase that can
100 assemble in the absence of TCAB1 is fully active, suggesting that TCAB1 is not necessary
101 for the enzymatic function of telomerase. Finally, analysis of the sub-cellular dynamics of
102 TCAB1 revealed that it rarely enters the nucleolus, suggesting that TCAB1 associates
103 with TR in the nucleoplasm and prevents its entry into the nucleolus rather than extracting
104 TR molecules from the nucleolus. Collectively, our results support a model in which
105 TCAB1 facilitates telomerase assembly by promoting nucleoplasmic accumulation of TR
106 to increase encounters with TERT which is also localized to the nucleoplasm.

107 Furthermore, we demonstrate that the nucleolar phase separation constitutes a barrier
108 for telomerase RNP assembly and suggest that incompletely assembled telomerase
109 RNPs are tightly associated with the nucleolus and do not readily enter the nucleoplasm.
110 Thus, cellular compartmentalization by phase-separated organelles such as the
111 nucleolus can directly regulate RNP function in human cells.
112

Results

Loss of TCAB1 leads to nucleolar accumulation of TR

To assess whether TR is sequestered in the nucleolus in the absence of TCAB1, we knocked out TCAB1 in HeLa cells and HeLa cells expressing 3xFLAG-HaloTag-TERT (Halo-TERT) using Cas9 with two guide RNAs to delete exons 2 and 3 from the TCAB1 gene, which removes the coding sequence for residues 144-214 of TCAB1 and results in a frame shift (Fig. S1A). TCAB1 knock-out was validated by Southern blot, PCR, western blot, and immunofluorescence imaging (IF, Fig. 1A-C, Fig. S1B-C). To assure that no truncated form of TCAB1 was expressed in TCAB1 knock-out cells, we analyzed TCAB1 expression using two antibodies, targeting the N-terminus and C-terminus of TCAB1, respectively (Fig. S1D). Both HeLa and Halo-TERT TCAB1 knock-out cell lines continuously grew at approximately 60% of the rate of their parental cell lines (Fig. 1D). Telomeres in cells lacking TCAB1 were stable over time at a shorter length than telomeres in control cells, as previously described (Fig. S1E) (Vogan et al., 2016). Fluorescence *in situ* hybridization (FISH) demonstrated that TR accumulated in the nucleolus in cells that lack TCAB1, as indicated by co-localization of TR and nucleolar dyskerin signals (Fig. 1C). To confirm the dyskerin signal marks nucleoli, we transiently expressed HaloTag-dyskerin and GFP-NPM1, a well-established marker of the granular component (GC) of the nucleolus, in control and TCAB1 knock-out cells. Dyskerin was enriched in nucleolar regions with low NPM1 intensity in the presence and absence of TCAB1 (Fig. S1F), consistent with previously observed localization of dyskerin to the dense fibrillar component (DFC) of the nucleolus (Yao et al., 2019). Importantly, expression of GFP-TCAB1 in TCAB1 knock-out cells rescued TR localization to Cajal bodies (Fig. 1E),

confirming that the miss-localization of TR to nucleoli is caused by absence of TCAB1. These observations demonstrate that TCAB1 is required to prevent TR accumulation in nucleoli.

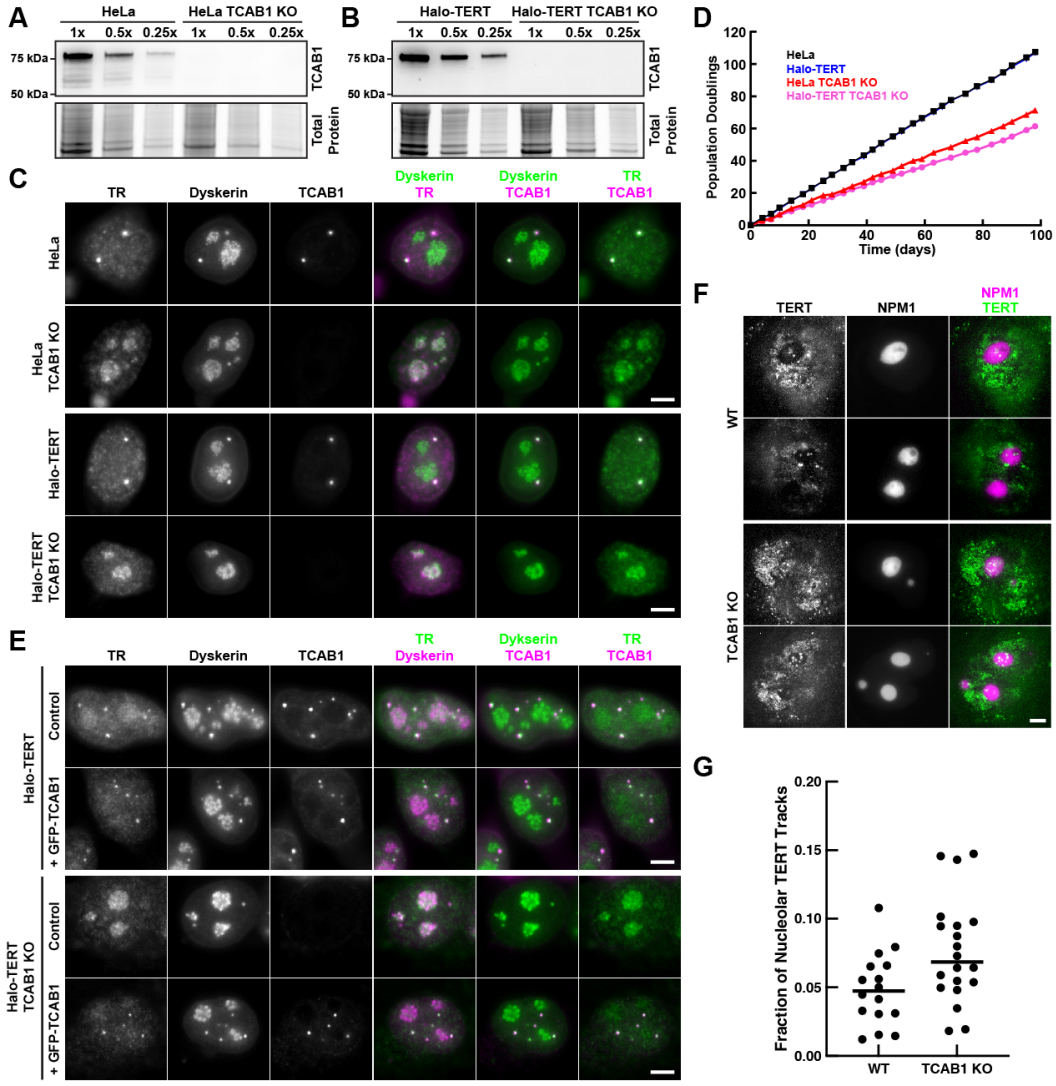

Figure 1. TR is localized to nucleoli in TCAB1 knock-out cells. (A-B) Western blot demonstrates the absence of TCAB1 protein in TCAB1 knock-out cell lines generated from **(A)** HeLa and **(B)** Halo-TERT parental cell lines (probed with Proteintech TCAB1 antibody). **(C)** Immuno-fluorescence with anti-dyskerin and anti-TCAB1 antibodies coupled to fluorescence in-situ hybridization with probes against TR, demonstrating the absence of TCAB1 and TR localization to nucleoli in TCAB1 knock-out cells (scale bar = 5 μm). **(D)** Growth rate of parental and TCAB1 knock-out cell lines. **(E)** Immuno-fluorescence with anti-dyskerin and anti-TCAB1 antibodies coupled to fluorescence in-situ hybridization with probes against TR, demonstrating that expression of GFP-TCAB1 in TCAB1 knock-out cells rescues TR localization to Cajal bodies (scale bar = 5 μm). **(F)** Maximum intensity projection (1000 frames at 10 ms per frame) of HaloTag-TERT (JFX650) in control and TCAB1 knock-out cells expressing GFP-NPM1 to mark nucleoli (scale bar = 5 μm). **(G)** Quantification of the fraction of TERT trajectories that overlap with the nucleolus in control and TCAB1 knock-out cells.

140 **TERT is not enriched in nucleoli in the absence of TCAB1**

141 Our previous observations demonstrated that TERT does not enter nucleoli in wild type
142 human cancer cells (Schmidt et al., 2016). To test whether TERT, like TR, is enriched in
143 nucleoli in the absence of TCAB1, we performed single-molecule imaging of 3xFLAG-
144 HaloTag-TERT in living HeLa and TCAB1 knock-out cell lines transiently expressing
145 GFP-NPM1 as a nucleolar marker. 3xFLAG-HaloTag-TERT was largely excluded from
146 the nucleolus in the presence and absence of TCAB1 with a small number of TERT
147 molecules localizing to nucleoli marker by NPM1 (Fig. 1F, Movies S1-2). Single-particle
148 tracking revealed that 4.9% and 7.7% of TERT trajectories overlapped with the nucleolus
149 in control and TCAB1 knock-out cells, respectively (Fig. 1G). To exclude the possibility
150 that nucleolar exclusion is a consequence of the 3xFLAG-HaloTag on the N-terminus of
151 TERT used in our experiments, we transiently expressed the 3xFLAG-HaloTag fused to
152 a nuclear localization sequence (NLS) in HeLa cells. Single-molecule imaging
153 demonstrated that the nuclear 3xFLAG-HaloTag signals overlapped with the nucleolus
154 (Fig. S1G-H, Movie S3). Similar to the 3xFLAG-HaloTag alone, 3xFLAG-HaloTag-
155 dyskerin also localized to the nucleolus (Fig. S1F). These results demonstrate that
156 3xFLAG-HaloTag-TERT is largely excluded from the nucleolus in the presence and
157 absence of TCAB1 and that this exclusion is not caused by the 3xFLAG-HaloTag but
158 instead is an intrinsic property of TERT. In contrast, TR accumulates in the nucleolus in
159 the absence of TCAB1 which demonstrates that the vast majority of TERT does not co-
160 localize with TR in cells lacking TCAB1 and therefore is not associated with TR.

161

162 **TCAB1 promotes telomerase RNP assembly**

163 Previous studies by other laboratories have concluded that telomerase assembly is
164 unaffected by the absence of TCAB1 and whether TCAB1 is required for telomerase
165 activity is controversial (Chen et al., 2018; Venteicher et al., 2009; Vogan et al., 2016).
166 Importantly, telomerase assembly was only qualitatively assessed in these studies. To
167 quantitatively analyze the role of TCAB1 in telomerase assembly, we immuno-purified
168 endogenous telomerase using a well-established anti-TERT antibody (Cohen et al.,
169 2007). The amount of TERT purified from TCAB1 knock-out cells was reduced compared
170 to control cells (Fig. 2A), which likely indicates a lower expression level of TERT in cells
171 lacking TCAB1. In contrast, TR levels were not reduced in cells lacking TCAB1 (Fig. 2B).
172 To quantify telomerase assembly, we measured TERT levels by western blot and
173 determined the amount of TR co-purified using Northern blot (Fig. 2A,B). The amount of
174 TR associated with TERT relative to total cellular TR was reduced to <20% in TCAB1
175 knock-out cells compared to parental controls (Fig. 2B-C). In addition, the ratio of TR
176 relative to TERT, which is a direct measure of telomerase assembly, was reduced to 20-
177 40% in cells lacking TCAB1 relative to controls (Fig. 2A-B,D). This excludes the possibility
178 that the lower amount of TR co-purified with TERT from TCAB1 knock-out cells is a
179 consequence of the reduction of total TERT immuno-precipitated from these cells (Fig.
180 2A,D). These observations strongly suggest that telomerase assembly is defective in cells
181 that lack TCAB1. To further test this hypothesis, we overexpressed TERT and TR in
182 parental and TCAB1 knock-out cells and immuno-purified TERT with the same TERT
183 antibody (Fig. 2E, Fig. S2A). After overexpression of TERT and TR, the fraction of TR

184 associated with TERT and the

185 ratio

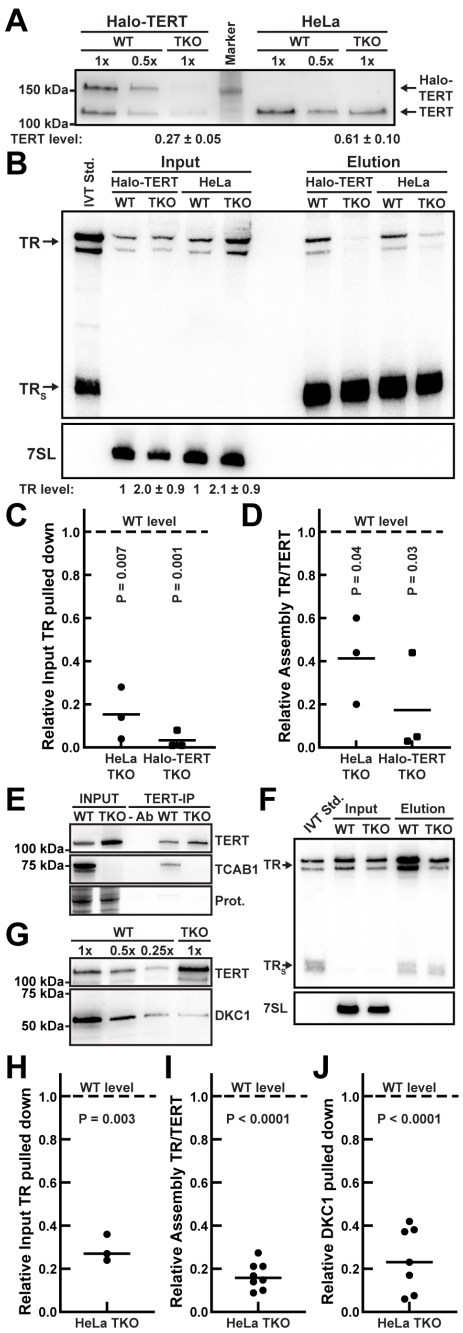

Figure 2. Telomerase Assembly is reduced in the absence of TCAB1. (A) Western blots analyzing endogenous TERT immuno-purification (using a sheep anti-TERT antibody) probed with a rabbit anti-TERT antibody (Abcam). TERT level normalized to WT (n = 3, SD). **(B)** Northern blot of RNA extracted from input and purified endogenous TERT samples probed with radiolabeled DNA oligonucleotides complementary to TR. Standards are *in vitro* transcribed full-length TR and truncated TR_S. TR_S was added to samples prior to RNA extraction as loading and recovery control. Input samples were also probed for 7SL RNA as loading control. Input TR levels relative to WT control normalized to 7SL RNA (n = 3, SD). **(C-D)** Quantification of the amount of **(C)** TR purified relative to input RNA levels, and **(D)** the ratio of TR relative to endogenous TERT in telomerase purified from TCAB1 knock-out cells compared to controls (n = 3, mean, T-Test). The dashed lines indicate the level in telomerase purified from wild-type TCAB1 cells which was normalized to 1.0. **(E-J)** TERT immuno-purification (using a sheep anti-TERT antibody) from HeLa control cells (WT) or TCAB1 knock-out cells (TKO) overexpressing TERT and TR. **(E)** Western blots of immuno-purified TERT probed with a rabbit anti-TERT antibody (Abcam) and an anti-TCAB1 antibody. **(F)** Northern blot of RNA extracted from input and purified TERT (Elution) probed with radiolabeled DNA oligonucleotides complementary to TR. Standards are *in vitro* transcribed full-length TR and truncated TR_S. TR_S was added to samples prior to RNA extraction as loading and recovery control. Input samples were also probed for 7SL RNA as loading control. **(G)** Western blots to analyze immuno-purified telomerase RNP composition. A single membrane was cut into two pieces that were probed with anti-TERT and anti-dyskerin antibodies, respectively. **(H-J)** Quantification of the amount of **(H)** TR relative to input TR (n = 3), **(I)** the ratio of TR to TERT (n = 8), and **(J)** dyskerin (n = 7) in TERT purifications from TCAB1 knock-out cells overexpressing TERT and TR compared to parental controls (mean, T-Test). The dashed lines indicate the level in telomerase purified from wild-type TCAB1 cells which was normalized to 1.0.

186

187 of TR relative to TERT were significantly reduced when telomerase was purified from

188 TCAB1 knock-out cells (Fig. 2E-F,H-I , Fig. S2B,D). Furthermore, the increased amount

189 of telomerase purified after over expression allowed us to assess the amount of dyskerin

190 associated with the telomerase RNP (Fig. 2G, Fig. S2C). Since TR bridges TERT and
191 dyskerin, dyskerin co-purified with TERT directly reports on the presence of TR.
192 Consistent with the reduction in TR, the amount of dyskerin bound to TERT was also
193 reduced to about 25% when TERT was purified from cells lacking TCAB1 compared to
194 parental controls (Fig. 2G, H, Fig. S2C,E). Importantly, we also confirmed that TCAB1
195 was absent from telomerase purified from TCAB1 knock-out cells (Fig. 2E, Fig. S2A).
196 Altogether, these results demonstrate that telomerase assembly is significantly reduced
197 (to ~20-40% of control levels) in the absence of TCAB1 and that overexpression of TERT
198 and TR is not sufficient to overcome this defect in telomerase RNP formation.

199 To assure that the reduction in telomerase assembly observed in TCAB1 knock-
200 out cells is not a consequence of an altered cell cycle distribution of cells that lacked
201 TCAB1, we purified telomerase from cells sychronized in various stages of the cell cycle.
202 Due to the slow growth of the TCAB1 knock-out cells a double thymidine block was not
203 feasible. We therefore synchronized cells using thymidine for 24 hours, released and
204 harvested cells immediately (early S phase), 4 hours (mid S phase), and 8 hours (G2/M
205 phase) after release. Cell-cycle synchronization was confirmed by DNA content analysis
206 using propidium iodide staining and flow cytometry (Fig. S2F). Telomerase assembly was
207 reduced in TCAB1 knock-out cells in all cell cycle stages analyzed (Fig. S2G-I). This
208 demonstrates that the reduction of telomerase assembly observed in cells lacking TCAB1
209 is not a consequence of an aberant cell-cycle distribution of TCAB1 knock-out cells.

210

211 **TCAB1 is not required for telomerase catalytic activity**

212 To assess whether TCAB1 plays a role in telomerase catalysis, we first analyzed the
213 enzymatic activity of endogenous telomerase purified from TCAB1 knock-out cells using
214 the direct telomerase extension assays (Fig. 3A,B). Consistent with previous results
215 (Chen et al., 2018), telomerase activity was strongly reduced in the absence of TCAB1
216 (Fig. 3C). To address whether this reduction in telomerase activity was a consequence of
217 the defect in telomerase assembly observed in TCAB1 knock-out cells, we determined
218 the specific activity of telomerase by dividing the measured activity by the amount of TR
219 present in the respective telomerase sample. Due to the very small amount of TR
220 detected in endogenous telomerase samples (Fig. 2B-C), the specific activity of
221 endogenous telomerase was highly variable in TCAB1 knock-out cells but did not appear
222 to be reduced compared to telomerase purified from control cells (Fig. S4A). To overcome
223 this limitation, we determined the specific activity of telomerase purified from cells
224 overexpressing TERT and TR. Similar to endogenous telomerase, activity of
225 overexpressed telomerase purified from HeLa and Halo-TERT cells lacking TCAB1 was
226 significantly reduced to 24% and 34% compared to controls, respectively (Fig. 3D-F, Fig.
227 S3). The specific activity of overexpressed telomerase purified from HeLa and Halo-TERT
228 cells lacking TCAB1 was slightly reduced (84% and 77% relative to control, respectively),
229 but this reduction was not statistically significant (Fig. 3G). Together these observations
230 demonstrate that net cellular telomerase activity is reduced in the absence of TCAB1,
231 while specific enzymatic activity is not. The reduction in cellular telomerase activity
232 corresponds closely to the reduction of telomerase assembly observed in TCAB1 knock-
233 out cells, suggesting that the smaller number of telomerase RNPs that form in the
234 absence of TCAB1 are fully active.

235

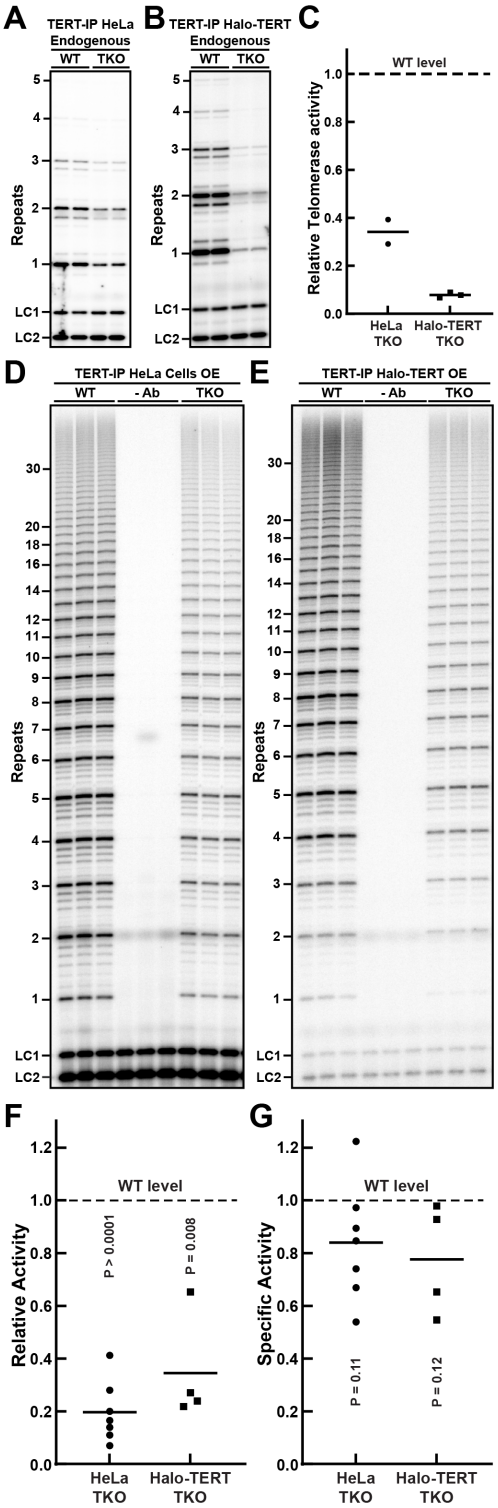

Figure 3. The specific activity of telomerase is unchanged in the absence of TCAB1. (A-B) Direct telomerase extension assay of endogenous telomerase immuno-purified from parental (WT) and TCAB1 knock-out (TKO) **(A)** HeLa and **(B)** Halo-TERT cell lines. Assays were carried out in the presence of 300 mM KCl and limiting amounts of dGTP. LC1 and LC2, radiolabeled DNA oligonucleotide loading controls. **(C)** Quantification of endogenous telomerase activity in samples from TCAB1 knock-out cells relative to parental controls (n = 3, mean). **(D-E)** Direct telomerase extension assay of overexpressed telomerase immuno-purified from parental (WT) and TCAB1 knock-out (TKO) **(D)** HeLa and **(E)** Halo-TERT cell lines. Assays were carried out in the presence of 150 mM KCl and 10 μM dATP, dTTP, and dGTP. LC1 and LC2, radiolabeled DNA oligonucleotide loading controls. In -Ab samples the TERT antibody was omitted during the immuno-purification. **(F)** Quantification of overexpressed telomerase activity in samples from TCAB1 knock-out cells relative to parental controls (n = 4-7, mean). **(G)** Specific activity of overexpressed telomerase purified from TCAB1 knock-out cells relative to parental controls (n = 4-7, mean, T-Test). Specific activity was calculated by dividing the relative activity (see Fig. 3F) by the relative amount of TR present in immuno-purified TERT samples (Fig. 2F). The dashed lines indicate the activity level in telomerase purified from wild-type TCAB1 control cells which was normalized to 1.0.

236

237

238 **TCAB1 mediates telomerase assembly in living cells**

239 The experiments presented thus far demonstrate that telomerase assembly is reduced in
240 the absence of TCAB1 but were carried out in fixed cells or cell lysates. To analyze
241 telomerase assembly in intact cells, we carried out live cell single-molecule imaging of
242 3xFLAG-HaloTag-TERT (Movie S4-5). We have previously demonstrated that there are
243 three distinct TERT populations in the nuclei of human cancer cells (Schmidt et al., 2016):
244 A static population (assembled telomerase RNPs bound to telomeres, Cajal bodies or
245 other cellular structures), a slowly diffusion population, and a rapidly diffusing population
246 (Fig. 4A). The slowly diffusing population likely includes assembled telomerase RNPs,
247 while the rapidly diffusing particles represents TERT molecules, which are not assembled
248 with TR (Fig. 4A). To determine the diffusion properties of TERT, when telomerase
249 assembly cannot occur, we knocked out TR. TR knock-out was confirmed by PCR and
250 Sanger sequencing, FISH, and qPCR (Fig. S4A-C). To define the diffusion rate of free
251 TERT molecules, we determined the diffusion coefficient of rapidly diffusing 3xFLAG-
252 HaloTag-TERT molecules in TR knock-out cells using the Spot-On tool, which calculates
253 the diffusion coefficient and the fraction of particles in each TERT population by fitting the
254 step-size distribution of TERT particles (Fig. 4A-B, Fig. S4D). Similarly, we defined the
255 rate of diffusion of assembled telomerase RNPs by measuring the diffusion coefficient of
256 slowly moving 3xFLAG-HaloTag-TERT molecules in control cells (Fig. 4A-B, Fig. S4D).
257 These measurements, in TR knock-out and control cells, are the most accurate
258 estimations possible for the diffusion coefficient of free TERT (D_{fast} = 1.9 ± 0.2 $\mu m^2/s$) and
259 TERT that is part of a telomerase RNP (D_{slow} = 0.35 ± 0.2 $\mu m^2/s$), respectively. Using the
260 diffusion coefficients, we fit the step-size distributions of

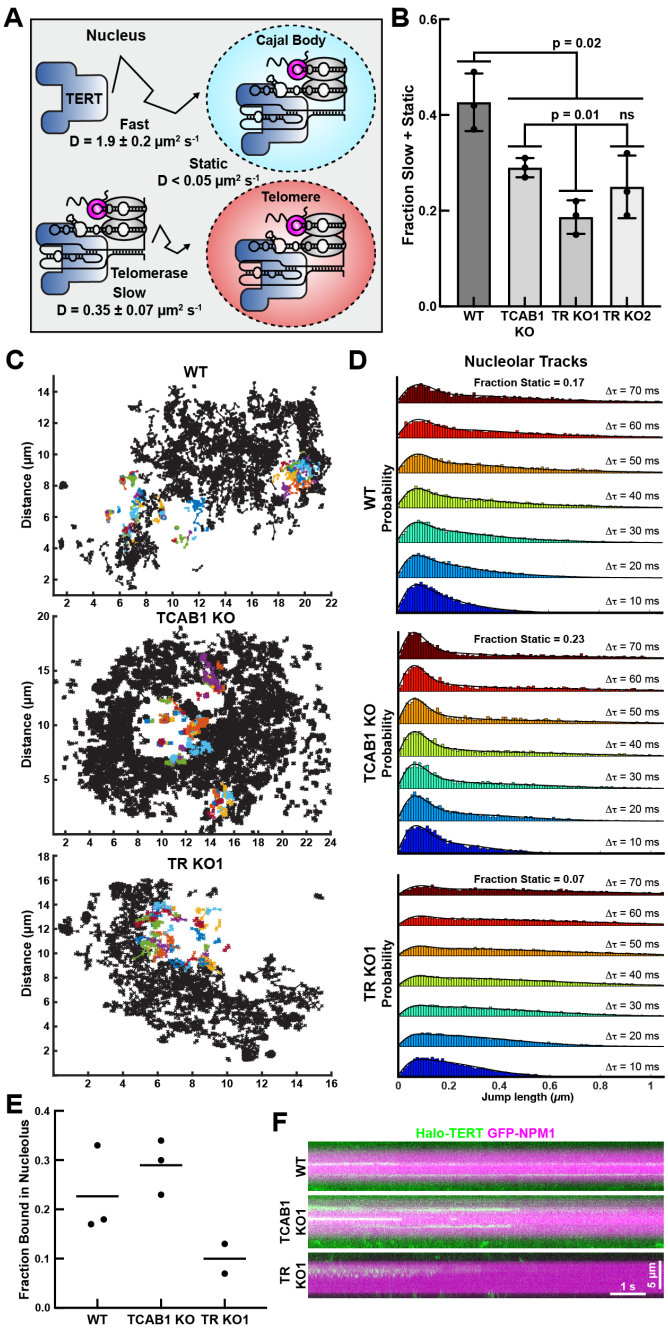

Figure 4. Telomerase assembly is reduced in live TCAB1 knock-out cells. (A) Diagram of distinct populations of TERT particles detected in control cells. Fast and slow diffusion coefficients were determined using Spot-On in control and TR knock-out cells, respectively (3 independent experiments, >15 cells per experiment per cell line, mean ± standard deviation). **(B)** Fraction of slow plus static TERT particles in control, TCAB1 knock-out, and TR knock-out cells expressing 3xFLAG-HaloTag TERT (3 independent experiments, >15 cells per experiment per cell line, mean ± standard deviation, t-test). **(C)** Graphs of HaloTag-TERT tracks that are nucleoplasmic (black) or overlap with the nucleolus for at least one frame (color) in control (WT), TCAB1 knock-out, and TR knock-out cells. **(D)** Probability density functions of the step-sizes derived from HaloTag-TERT molecules that overlap with the nucleolus for at least one frame and the corresponding 3-state model fit using the SpotOn tool (pooled data from 3 independent experiments, >18 cells total per cell line). **(E)** Quantification of the fraction of TERT particles statically bound to the nucleolus in control (WT), TCAB1 knock-out, and TR knock-out cells (2-3 independent experiments, >18 cells per experiment per cell line). **(F)** Kymographs of HaloTag-TERT particles that colocalized with nucleoli marked by GFP-NPM1 in control (WT), TCAB1 knock-out, and TR knock-out cells (also see Movies S5).

TERT trajectories in control, TR knock-out, and TCAB1 knock-out cells to determine the fraction of TERT molecules in the fast, slow, and static TERT populations. Our key assumption is that rapidly diffusing TERT particles represent free TERT, while the much larger telomerase RNP is part of the slowly moving and static TERT populations. Consistent with this assumption, the fraction of TERT particles in the slowly diffusing and

267 static populations was significantly reduced in TR knock-out cells (19 ± 4 %, 25 ± 7 %)
268 compared to control cells (43 ± 6 %) (Fig. 4B). It is important to note that, even in TR
269 knock-out cells, 19-25% of TERT particles are slowly diffusing or static (Fig. 4B). Because
270 TR is absent in these cells, the slowly diffusing and static TERT molecules must be the
271 result of interactions of TERT with cellular components other than Cajal bodies or
272 telomeres. Importantly, we also observed a significant reduction in the fraction of slowly
273 diffusing and static TERT particles in TCAB1 knock-out cells (29 ± 2 %) compared to
274 control cells (43 ± 6 %) (Fig. 4B), consistent with a defect in telomerase assembly when
275 TCAB1 is absent. The fraction of slowly diffusing and static TERT particles in TCAB1
276 knock-out cells (29 ± 2 %) was higher than in TR knock-out cells (19 ± 4 %, 25 ± 7 %),
277 suggesting that telomerase assembly is strongly reduced but not completely lost in the
278 absence of TCAB1, which is consistent with our telomerase assembly analysis using
279 purified telomerase (Fig. 3). In addition, in the absence of TCAB1, the reduction of
280 telomerase assembly was only detected for TERT particles that localized to the
281 nucleoplasm but not the nucleolus (Fig. 4C-D, Fig. S4E).

282 Because stable binding of telomerase to the telomere requires base-pairing of TR
283 with the single-stranded telomeric overhang (Schmidt et al., 2018), we analyzed the
284 interaction of TERT with telomeres. To assess TERT association with telomeres, we
285 plotted the step size of TERT trajectories vs. the distance from the closest telomere for
286 each step of these trajectories (Fig. S5A). In control cells, we observed an enrichment of
287 smaller step sizes and particles in close proximity to telomeres, consistent with TERT
288 interactions with the chromosome end (Fig. S5A). In contrast, TERT trajectories in TCAB1
289 knock-out cells lacked this enrichment, and the step size vs. distance from the closest

290 telomere plots were identical to those from TR knock-out cells (Fig. S5A). Next, we filtered
291 out TERT trajectories that came into proximity with telomeres marked by mEOS3.2-TRF2,
292 as previously described (Schmidt et al., 2016). Diffusion analysis of these TERT
293 trajectories using SpotOn revealed that the fraction of static TERT particles at telomeres
294 was reduced from 12% in control cells to 4-5% in TCAB1 and TR knock-out cells (Fig.
295 S5B). These observations indicate that, in the absence of either TCAB1 or TR, stable
296 interactions of telomerase with telomeres occur at a lower frequency, because they
297 require TR to stably bind to the chromosome end (Schmidt et al., 2018). Together these
298 single-molecule imaging experiments demonstrate that in living cells, telomerase
299 assembly is significantly reduced in the absence of TCAB1.
300

301 **TERT is not retained in the nucleolus in the absence of TR**

302 The experiments presented thus far have demonstrated that telomerase assembly is
303 reduced in cell lysates and in living cells when TCAB1 is absent, but do not address the
304 sub-cellular localization of telomerase assembly. It was previously suggested that
305 telomerase is assembled in the nucleolus and active telomerase is enriched in the
306 nucleolus in the absence of TCAB1 (Lee et al., 2013). Alternatively, TERT could associate
307 with TR outside of the nucleolus and a small fraction of the telomerase RNP could localize
308 to the nucleolus after assembly. Importantly, telomerase assembly within the nucleolus
309 would require TERT to localize to the nucleolus independently of TR. To address whether
310 TERT can enter the nucleolus in the absence of TR, we analyzed TERT trafficking at the
311 single-molecule level in TR knock-out cells synchronized in S-phase of the cell cycle.
312 Nucleoli were marked by transient expression of GFP-NPM1. As described above (Fig.

313 1F, Movies 1-2), a very small fraction of TERT particles were detected within the nucleolus
314 in control and TCAB1 knock-out cells. Analysis of the diffusion properties of TERT
315 particles co-localized with GFP-NPM1 revealed that the fraction of static TERT molecules
316 was slightly increased in TCAB1 knock-out cells (29%) compared to controls (23%, Fig.
317 4C-F). In contrast, static TERT molecules that co-localized with the nucleolus were less
318 frequently detected in TR knock-out cells (10%, Fig. 4C-F, Movie S6). Interestingly, we
319 did observe very rare TERT molecules in TR knock-out cells that were mobile but
320 constrained within a sub region of the nucleolus which, based on our other observations,
321 likely corresponds to TERT within the DFC that is not bound to TR (Fig. 4D, Movie S6).
322 In total, these results demonstrate that, though rare, TERT can enter the nucleolus
323 independently of TR but does not transition into a stably bound state that likely requires
324 association with TR.
325
326 **TCAB1 is excluded from the nucleolus**
327 Our experiments demonstrate that the loss of TCAB1 leads to an accumulation of TR in
328 the nucleolus (Fig. 1). TCAB1 could lead to the depletion of TR from the nucleolus by
329 binding to TR that has dissociated from the nucleolus and preventing it from re-entering.
330 Alternatively, TCAB1 could bind to TR within the nucleolus and accelerate the export of
331 TR from the nucleolus, which requires TCAB1 entry into the nucleolus. To analyze the
332 sub-nuclear localization of TCAB1, we introduced a 3XFLAG-HaloTag at the endogenous
333 *TCAB1* locus and generated single-cell clones that exclusively expressed 3XFLAG-
334 HaloTag-TCAB1 (Fig. 5A). HaloTag-TCAB1 strongly accumulated at Cajal bodies
335 (marked by BFP-coilin) and was excluded from the nucleolus (Fig. 5B, Movie S7).

336 Surprisingly, a large fraction of HaloTag-TCAB1 localized to the cytoplasm, suggesting
337 that its import into the nucleus is restricted (Fig. 5B). To assure that the cytoplasmic
338 localization of HaloTag-TCAB1 was not an artifact of fusing TCAB1 to the HaloTag, we
339 carried out cell fractionation experiments, which demonstrated that untagged TCAB1 was
340 also detected in the cytoplasm and the nucleus but was not located in the nucleolus (Fig.
341 5C), consistent with our imaging experiments. Single-particle tracking of HaloTag-TCAB1
342 within the nucleus revealed that the diffusion dynamics of TCAB1 were similar to those of
343 TERT (Fig. 4B, Fig. 5D). Like TERT, the step size distribution of HaloTag-TCAB1 particles
344 fit well to a three-state model (Fig. 5D). The freely diffusing state of TCAB1 had a higher
345 diffusion coefficient than TERT (D_{fast} = 2.4 $\mu m^2/s$ vs. 1.9 $\mu m^2/s$). Strikingly, the diffusion
346 coefficient of the slowly diffusing state for TCAB1 and TERT were identical (D_{slow} = 0.35
347 $\mu m^2/s$), consistent with TCAB1 and TERT being part of assembled H/ACA RNPs. On rare
348 occasions, we observed HaloTag-TCAB1 molecules that associated with the nucleolus
349 (Fig. 5E, Movie S7-8). In contrast, single HaloTag-dyskerin were readily detected stably
350 bound to the nucleolus (Fig. 5F-G). In total, these results demonstrate that TCAB1 is
351 largely excluded from the nucleolus and that TCAB1 molecules diffuse through the
352 nucleoplasm at a rate similar to assembled telomerase RNPs.

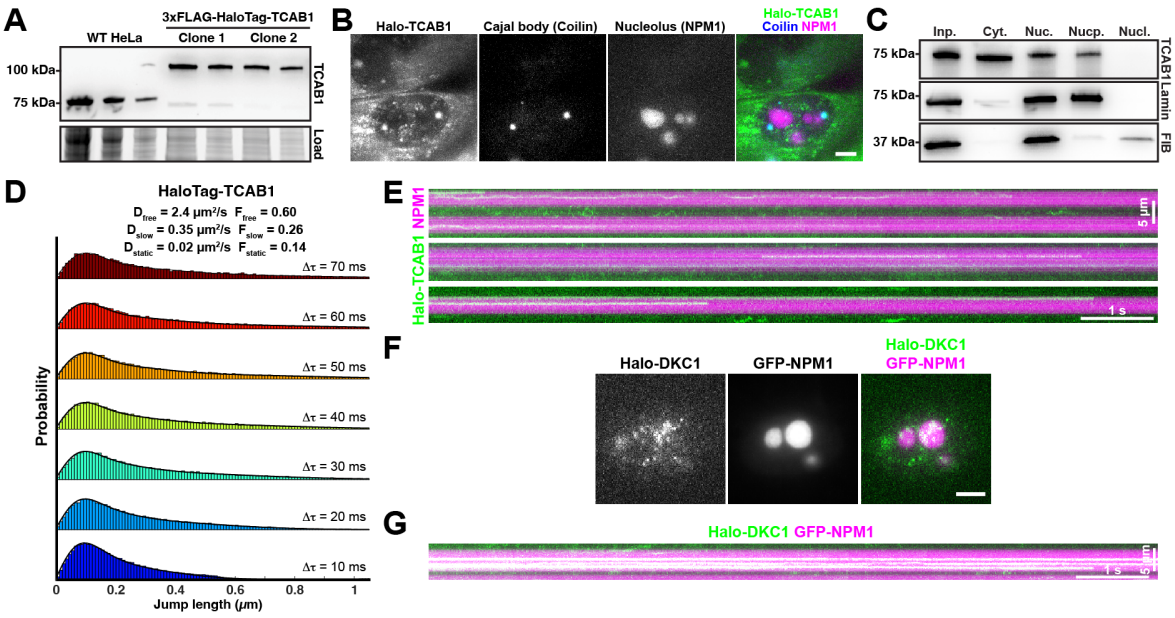

Figure 5. TCAB1 is excluded from the nucleolus. (A) Western blot probed with an antibody against TCAB1 demonstrating the exclusive expression of HaloTag-TCAB1 in genome edited Hela cells. **(B)** Maximum intensity projection of a single-molecule imaging movie of HaloTag-TCAB1 labeled with JFX650 in cells transiently expressing BFP-coilin and GFP-NPM1 to mark Cajal bodies and nucleoli, respectively (scale bar = 5 μm) **(C)** Western blots of samples of cellular fractionation experiments (left to right: Input, Cytoplasm, Nucleus, Nucleoplasm, Nucleolus) from HeLa cells. Blots were probed with antibodies against TCAB1, fibrillarin (nucleolar marker), and lamin B1 (nucleoplasmic marker). **(D)** Probability density functions of the step-sizes derived from nuclear HaloTag-TCAB1 trajectories and the corresponding 3-state model fit using the SpotOn tool (pooled data from 2 biological replicates of two independent HaloTag-TCAB1 clones, >10 cells total per replicate). **(E)** Kymograph of nucleolar HaloTag-TCAB1 particles over time. **(F)** Live cell fluorescence images of single 3xFLAG-HaloTag-dyskerin particles, nucleoli marked by GFP-NPM1 (scale bar = 5 μm). **(F)** Kymograph of nucleolar 3xFLAG-HaloTag-dyskerin particles over time.

The majority of TR is tightly associated with the nucleolus in absence of TCAB1

Single-molecule imaging of TERT revealed that <10% of TERT molecules localize to the nucleolus in control and TCAB1 knock-out cells (Fig. 1G). To determine what fraction of TR associates with the nucleolus in the absence of TCAB1, we carried out cellular fractionations to isolate nucleoli. Nucleoli were purified by rupturing isolated nuclei via sonication, followed by centrifugation through a high-density sucrose cushion (Lam and Lamond, 2006). Isolated nucleoli were enriched with the nucleolar protein fibrillarin and

362 U3 snoRNA while being depleted of lamin B1 and the 7SK RNA (Fig. 6A,B), which serve
363 as nucleoplasmic markers, demonstrating that we successfully purified nucleoli using this
364 approach. To determine the amount of TR found in the nucleolus and the nucleoplasm,
365 we quantified the level of TR relative to that of the U3 or the 7SK RNA, respectively. In
366 control cells, the majority of TR was found in the nucleoplasmic fraction, and a small
367 amount of TR was detected in nucleoli (Fig. 6B), consistent with previous work that
368 analyzed TR localization by live cell imaging (Laprade et al., 2020). In contrast, in TCAB1
369 knock-out cells, TR was depleted from the nucleoplasm and enriched in the nucleolus
370 (Fig. 6B,C). To assess the impact of high salt concentrations, used by others to extract
371 telomerase from human cells (Chen et al., 2018), on nucleolar integrity, we supplemented
372 ruptured nuclei with potassium chloride, prior to isolating nucleoli. After exposure to a high
373 salt concentration, fibrillarin and TR were found in the nucleoplasmic fraction instead of
374 the nucleolar pellet (Fig. S6), demonstrating that nucleoli are disrupted, and TR is
375 released when exposed to non-physiological salt concentrations. These observations
376 confirm that >50% of TR is sequestered in the nucleolus in the absence of TCAB1 and
377 strongly suggest that TR is tightly associated with the nucleolus under these
378 circumstances, preventing it from entering the nucleoplasm.

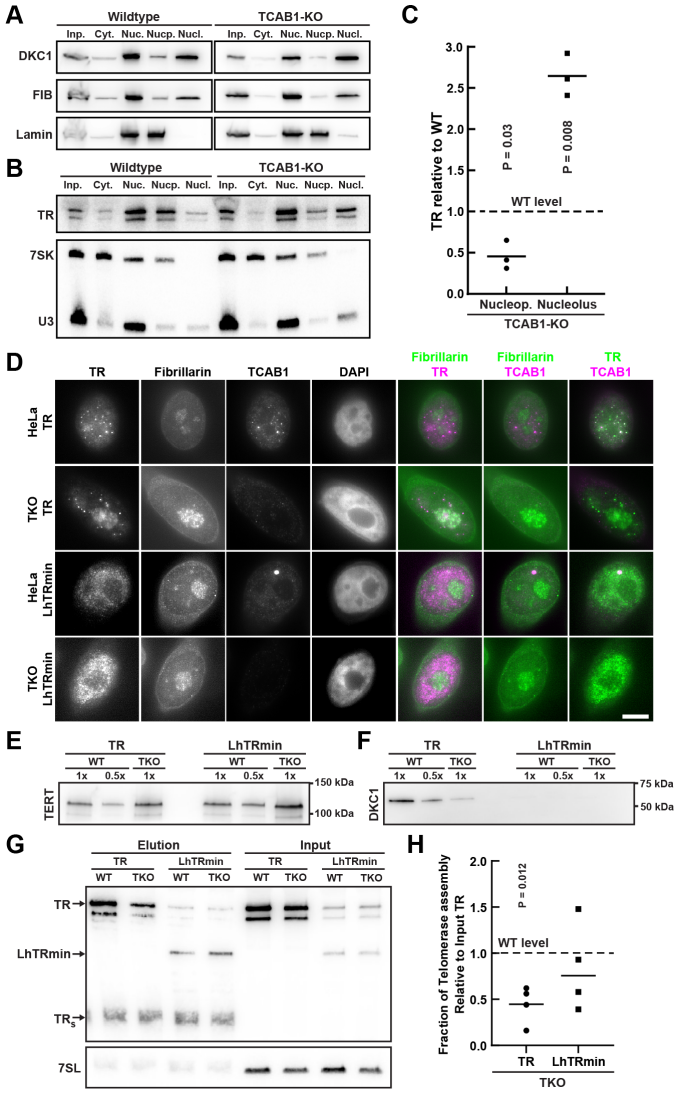

Figure 6. Localization of TR to the nucleoplasm rescues telomerase assembly in the absence of TCAB1. (A) Western blots of samples of cellular fractionation experiments (left to right: Input, Cytoplasm, Nucleus, Nucleoplasm, Nucleolus) from control and TCAB1 knock-out cells. Blots were probed with antibodies against dyskerin, fibrillarin (nucleolar marker), and lamin B1 (nucleoplasmic marker). **(B)** Northern blots of samples of cellular fractionation experiments (left to right: Input, Cytoplasm, Nucleus, Nucleoplasm, Nucleolus) from control and TCAB1 knock-out cells. Blots were first probed with radiolabeled DNA oligonucleotides complementary to TR, followed by probes complementary to the 7SK RNA (nucleoplasmic marker) and the U3 snoRNA (nucleolar marker). **(C)** Quantification of the nucleoplasmic and nucleolar abundance of TR in TCAB1 knock-out cells relative to control cells. Nucleoplasmic TR signal was normalized to the 7SK RNA signal and nucleolar TR signal was normalized to the U3 RNA signal (n = 3, mean, T-Test). **(D)** IF-FISH of control and TCAB1 knock-out cells over-expressing TERT and full-length TR or LhTRmin probed with antibodies for fibrillarin and TCAB1 and anti TR-FISH probes (scale bar = 5 µm). **(E-F)** Western blots or TERT immuno-purified from control and TCAB1 knock-out cells expressing TERT and full-length TR or LhTRmin probed with antibodies for **(E)** TERT and **(F)** dyskerin. **(G)** Northern blot of RNA extracted from input and TERT samples purified from control and TCAB1 knock-out cells expressing TERT and full-length TR or LhTRmin. Standards are *in vitro* transcribed full-length TR and truncated TR_S. Input samples were also probed for 7SL RNA as loading control. **(H)** Quantification of TR or LhTRmin associated with TERT relative to input RNA of TERT samples purified from TCAB1 knock-out cells compared to control cells.

Localization of the telomerase RNA to the nucleoplasm rescues telomerase assembly in the absence of TCAB1

Our data demonstrate that stable association of TERT with the nucleolus requires its interaction with TR (Fig. 4). Importantly, we cannot distinguish whether static TERT molecules within the nucleolus represent telomerase RNPs that have assembled in the nucleolus or the nucleoplasm. To address whether the telomerase RNP can assemble in

388 the nucleoplasm, we expressed a truncate version of TR (LhTRmin) that lacks the H/ACA
389 domain which binds to dyskerin and TCAB1 and therefore does not localize to the
390 nucleolus or Cajal bodies (Fig. 6D) (Vogan et al., 2016). Consistent with our results shown
391 above, assembly of TERT with full-length TR and dyskerin was significantly reduced in
392 the absence of TCAB1 (Fig. 6E-H). In contrast, TERT association with LhTRmin was not
393 significantly different in TCAB1 knock-out cells compared to control cells expressing
394 LhTRmin (Fig. 6E-H). Importantly, no dyskerin was associated with TERT purified from
395 cells expressing LhTRmin (Fig. 6F). These results demonstrate that forcing TR
396 localization to the nucleoplasm suppresses the telomerase assembly defect observed in
397 TCAB1 knock-out cells and indicate that the telomerase RNP can form outside of the
398 nucleolus. Importantly, these observations suggest that the sequestration of TR in the
399 nucleolus causes the reduction in telomerase assembly observed in the absence of
400 TCAB1.
401
402 **Analysis of nucleolar telomerase RNA and snoRNP dynamics**
403 The results presented thus far have demonstrated that TR accumulates in nucleoli in the
404 absence of TCAB1 by cell fractionation and in fixed cells, but we have not addressed the
405 dynamic localization of TR in living cells. Since TR is targeted to nucleoli by dyskerin and
406 other H/ACA RNP components, we first used dyskerin as a surrogate for TR and H/ACA
407 snoRNPs in general. We transiently expressed HaloTagged dyskerin in parental HeLa
408 and TCAB1 knock-out cells and analyzed dyskerin binding to the nucleolus using
409 fluorescence recovery after photobleaching (FRAP). We identified cells with two clearly
410 visible nucleoli, completely photo-bleached the dyskerin signal in one of the nucleoli and

411 quantified the recovery of the fluorescence signal (Fig. 7A, Movies S9-10). The dyskerin
412 signal recovered rapidly ($t_{1/2}$ = 28 s) but only ~65% of the signal was recovered after > 4
413 minutes (Fig. 7B-D, Movies 9-10). This indicates that there are at least two distinct
414 populations of dyskerin molecules in the nucleolus, a rapidly exchanging population and
415 a static population that does not dissociate from the nucleolus over the time course of this
416 experiment (Fig. 7D). The presence of a mobile dyskerin population was confirmed by
417 analysis of the unbleached nucleolus, which lost fluorescence signal with similar kinetics
418 (Fig. 7A, Fig. S7A-B). Importantly, no significant difference in dyskerin dynamics were
419 observed in TCAB1 knock-out cells compared to parental controls (Fig. 7A-D, Fig. S7A-
420 B), which indicates that TCAB1 is not required to extract dyskerin-containing scaRNPs
421 from nucleoli.

422 To directly analyze the dynamics of TR binding to the nucleolus in the absence of
423 TCAB1, we introduced three MS2 stem loops at the 5' end of the endogenous TR gene
424 (Fig. 7E-G), as previously described (Laprade et al 2020). This approach allowed us to
425 visualize TR in living cells using the MS2 coat protein (MCP) fused to the mNeonGreen
426 fluorescent protein, stably expressed by lentiviral transduction (Fig. 7E). Similar to
427 endogenous TR (Fig. 1), 3xMS2-TR localized to nucleoplasmic foci in control cells (likely
428 Cajal bodies) and to nucleoli in absence of TCAB1 (Fig. 7H, Fig. S7C). Like dyskerin (Fig.
429 S1F), MS2-TR was specifically enriched in nucleolar regions with reduced granular
430 component marker (BFP-NLS, Fig. S1F) intensity in the absence of TCAB1 (Fig. 7H,
431 zoomed panel), which corresponds to the DFC of the nucleolus. To measure the
432 dynamics of TR association with the nucleolus in TCAB1 knock-out cells, we carried out
433 FRAP experiments of MCP-mNeonGreen bound MS2-TR clearly localized within DFC of

434 the nucleolus (Fig. 7I). After bleaching nucleolar MS2-TR enriched in the DFC in TCAB1
435 knock-out cells, ~40% of the fluorescence recovered with a halftime of recovery of ~50
436 seconds (Fig. 7I-L). This demonstrates that, in the absence of TCAB1, the majority of TR
437 is tightly associated with the nucleolus and the remaining TR molecules exchange with
438 the nucleoplasm with kinetics comparable to dyskerin. In total, these results strongly
439 suggest that the reduction of telomerase assembly, observed in the absence of TCAB1,
440 is a consequence of the sequestration of TR in the nucleolus, where it infrequently
441 encounters TERT which is largely localized to the nucleoplasm.

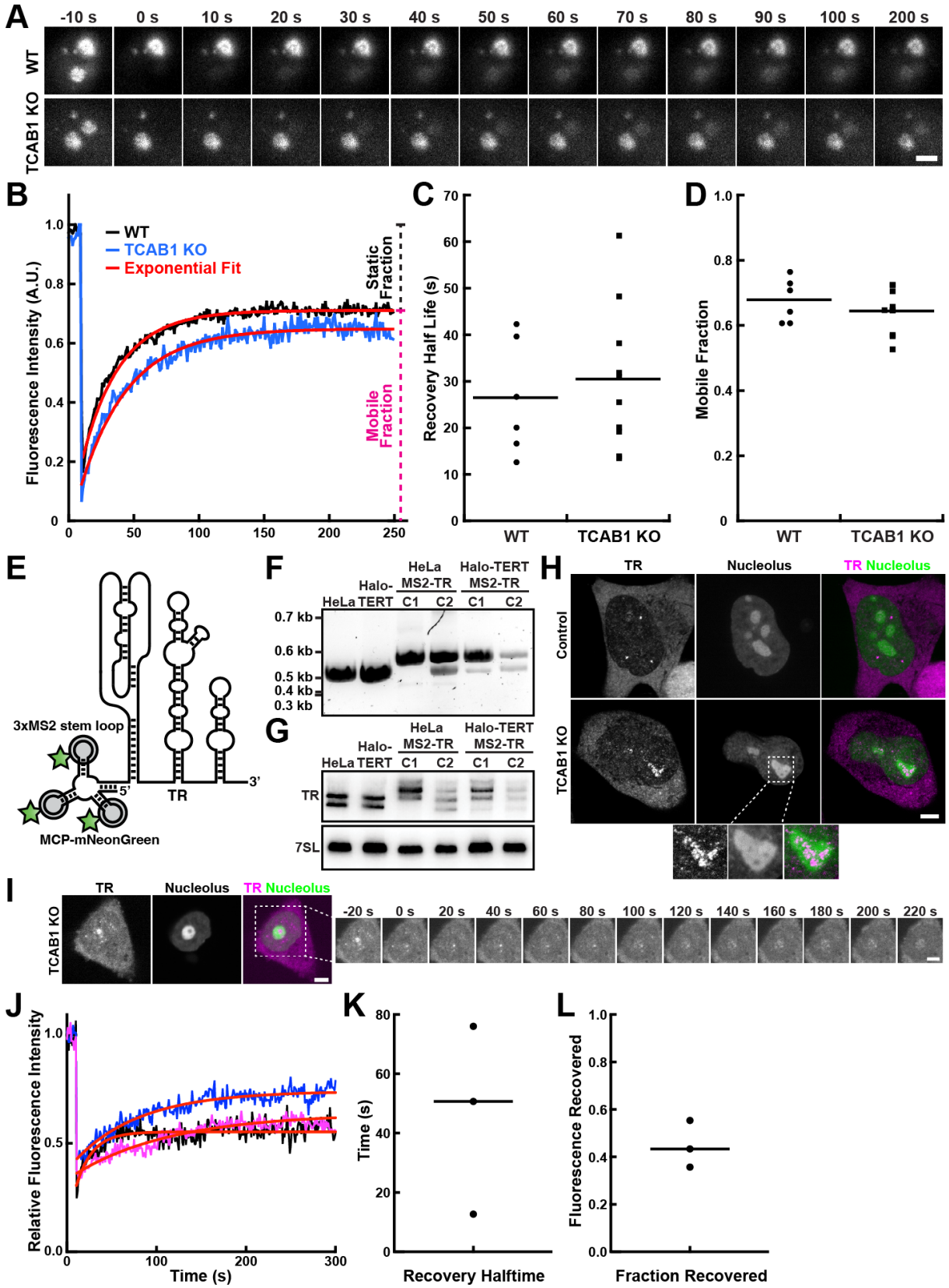
A
-10 s
0 s
10 s
20 s
30 s
40 s
50 s
60 s
70 s
80 s
90 s
100 s
200 s
WT
TCAB1 KO
B
WT
TCAB1 KO
Exponential Fit
Static Fraction
Mobile Fraction
Fluorescence Intensity (A.U.)
C
Recovery Half Life (s)
WT
TCAB1 KO
D
Mobile Fraction
WT
TCAB1 KO
E
3xMS2 stem loop
5'
3'
TR
MCP-mNeonGreen
F
HeLa
Halo-TERT
Halo-TERT MS2-TR
C1
C2
0.7 kb
0.6 kb
0.5 kb
0.4 kb
0.3 kb
G
TR
7SL
H
TR
Nucleolus
TR Nucleolus
Control
TCAB1 KO
I
TR
Nucleolus
TR Nucleolus
TCAB1 KO
-20 s
0 s
20 s
40 s
60 s
80 s
100 s
120 s
140 s
160 s
180 s
200 s
220 s
J
Relative Fluorescence Intensity
Time (s)
K
Time (s)
Recovery Halftime
L
Fluorescence Recovered
Fraction Recovered

442

Figure 7. Analysis the nucleolar binding dynamics of dyskerin and TR. (A) Images of control and TCAB1 knock-out cells expressing 3xFLAG-HaloTag-dyskerin before and after photobleaching of nucleolar dyskerin (JFX650, scale bar = 5 µm). **(B)** Fluorescence recovery curves of nucleolar dyskerin in control and TCAB1 knock-out cells. Data was fit with a single exponential function. **(C)** Quantification of half-life of fluorescence recovery, calculated from the rate constant of the single exponential fit of the data shown in Fig. 7B (n = 6 and 9, mean). **(D)** Quantification of the mobile fraction of nucleolar dyskerin based on the single exponential fit of the data shown in Fig. 7B (n = 6 and 9, mean). **(E)** Model of 3xMS2-TR bound to MCP-mNeonGreen. **(F)** PCR analysis of the endogenous TR locus after insertion of the 3xMS2 sequence. **(G)** Northern blot probed with radioactively labeled anti-TR oligonucleolides of control cells and genome edited clones expressing 3xMS2-TR. **(H)** Live cell microscopy images of control and TCAB1 knock-out cells expressing 3xMS2-TR, MCP-mNeonGreen, and BFP-NLS to mark the nucleolus. Zoomed images demonstrate the enrichment of TR in the DFC indicated by low BFP-NLS signal within the nucleolus. **(I)** FRAP of 3xMS2-TR within the DFC of the nucleolus marked by BFP-NLS. **(J)** FRAP curves and single exponential fits of the data (red). **(K)** Quantification of the recovery halftime from single-exponential fits of the recovery curves show in (I). **(L)** Quantification of the fraction of fluorescence recovered from single-exponential fits of the FRAP curves show in (I).

443

444

445 **Discussion**

446 The experiments described in this study demonstrate that TCAB1 promotes telomerase
447 assembly. In the absence of TCAB1, the telomerase RNA is targeted to the nucleolus via
448 its association with dyskerin and other components of the H/ACA complex. In contrast to
449 TR, TERT rarely enters the nucleolus, preventing its association with TR in cells that lack
450 TCAB1. In addition, we demonstrate that TCAB1 does not enter nucleoli excluding the
451 possibility that TCAB1 extracts TR containing RNPs from nucleoli. These observations
452 suggest that nuclear compartmentalization, which is a consequence of nucleolar phase
453 separation, counteracts telomerase assembly. Our analysis of the dynamic association
454 of dyskerin bound snoRNPs and TR with nucleoli revealed that a significant fraction of
455 TR containing RNPs and snoRNPs in general are tightly associated with the nucleolus.
456 Finally, we demonstrate that while telomerase assembly is limited, the specific activity of
457 telomerase is unchanged in the absence of TCAB1, which excludes a role of TCAB1 in
458 telomerase catalytic function. Altogether our work supports an entirely new hypothesis for
459 the role of TCAB1 in telomerase function in human cells and provides insight into the role
460 phase-separated organelles play in RNA dynamics and RNP assembly and function.

461

462 **TCAB1 promotes telomerase assembly**

463 The importance of TCAB1 for telomere synthesis is undisputed (Chen et al., 2018;
464 Venteicher et al., 2009). Knock-out or depletion of TCAB1 results in telomere shortening
465 (Chen et al., 2018; Venteicher et al., 2009; Vogan et al., 2016). All previous work also
466 concluded that TR is enriched in the nucleolus in the absence of TCAB1 (Chen et al.,
467 2018; Stern et al., 2012; Vogan et al., 2016; Zhong et al., 2011). However, prior studies

468 conclude that TCAB1 is not required for telomerase assembly but instead plays a role in
469 telomerase trafficking to Cajal bodies and telomeres or is required for telomerase
470 catalysis (Chen et al., 2018; Stern et al., 2012; Venteicher et al., 2009; Vogan et al., 2016;
471 Zhong et al., 2011). In contrast, our results demonstrate that, in the absence of TCAB1,
472 telomerase assembly is significantly reduced. This finding is supported by two completely
473 distinct and complementary approaches. First, we purified TERT from cell lysates and
474 demonstrated that the fraction of TR associated with TERT is reduced to 20-40% in the
475 absence of TCAB1 compared to control cells. Secondly, we used the single-molecule
476 diffusion dynamics of TERT as a read-out of telomerase assembly. When telomerase
477 assembly is impossible (in TR knock out cells), the vast majority (~75-80%) of TERT
478 molecules rapidly diffuse through the nucleus. In contrast, in the presence of TR, only
479 ~55% of TERT molecules rapidly diffuse through the nucleus, because the association of
480 TERT with TR leads to the formation of a large RNP that moves through the nucleus at a
481 slower rate. In the absence of TCAB1, the fraction of rapidly moving TERT molecules is
482 significantly increased to ~70%, consistent with a reduction in telomerase assembly.
483 Assuming a maximal change of 25% in the fraction of rapidly diffusing TERT molecules
484 (from 55% in wild type to 80% in TR knock-out cells), the 15% increase, observed in the
485 absence of TCAB1 compared to wild type, corresponds to a 60% reduction (15/25) in
486 telomerase assembly, which is consistent with our results obtained by purifying
487 telomerase from cell lysates. In addition, we demonstrate that the TERT less frequently
488 forms stable interactions with telomeres in the absence of TCAB1, consistent with fewer
489 TERT molecules being bound to TR. The reduction in telomerase assembly in cells
490 lacking TCAB1 leads to a lower number of telomerase RNPs per cell and in turn telomere

491 shortening. Importantly, telomerase assembly is reduced but not completely abolished
492 when TCAB1 is absent, which is sufficient to support continuous cell proliferation with a
493 short telomere length set point.
494
495 **TCAB1 is not required for telomerase catalysis**
496 Previous work by others has reported conflicting results regarding the role of TCAB1 in
497 telomerase catalysis, ranging from full enzymatic activity in initial reports to substantial
498 activity defects in the most recent study (Chen et al., 2018; Venteicher et al., 2009; Vogan
499 et al., 2016). Importantly, both our work and the only other study that analyzed the role of
500 TCAB1 in telomerase activity using the "gold-standard" direct telomerase extension assay
501 concluded that telomerase activity is significantly reduced in the absence of TCAB1.
502 While both studies concur on the degree to which telomerase activity is reduced in the
503 absence of TCAB1, the proposed underlying molecular mechanisms differ. Chen *et al*.
504 propose that TCAB1 is required for proper folding of the CR4/CR5 region of the
505 telomerase RNA, which directly associates with TERT, without affecting telomerase
506 assembly (Chen et al., 2018). Recent structural analysis of the telomerase RNP from
507 human cells revealed that TCAB1 is located far away from the CR4/CR5 region of TR
508 (Ghanim et al., 2021). Although it is possible that telomerase can adopt additional
509 conformations, based on the currently available structural information it is difficult to
510 rationalize a molecular mechanism by which TCAB1 could specifically promote CR4/CR5
511 folding. In addition, due to the misfolding of TR telomerase was proposed to adopt a low
512 activity state in the absence of TCAB1. Experimentally such a low activity state would
513 manifest itself as a reduction in the specific activity of telomerase (telomerase activity per

514 assembled telomerase RNP). Our experiments strongly suggest that, while telomerase
515 assembly is reduced in the absence of TCAB1, the limited amount of telomerase that can
516 assemble is close to fully active (i.e. does not have reduced specific activity). One
517 possible explanation for the discrepancies between the work by Chen *et al*. and our study
518 is the methodology used to generate cell lysates. Our results demonstrate that the high
519 salt concentration used by Chen *et al.* to generate nucleolar extracts dissolves nucleoli
520 and releases TR (Fig. 6). Consistent with this observation, salt concentrations > 250 mM
521 have been shown to disrupt the phase separation phenomena underlying the formation
522 of the nucleolus (Feric et al., 2016). Solubilization of the nucleolus and release of TR
523 would override the localization of TR and TERT to distinct sub-cellular compartments and
524 could allow telomerase to assemble in the nuclear extract. Importantly, our single-
525 molecule imaging of TERT dynamics is consistent with a reduction of telomerase
526 assembly in intact cells. Altogether, our enzymatic analysis, and the positioning of TCAB1
527 within the telomerase RNP do not support a role of TCAB1 in TR folding and telomerase
528 catalysis but are fully consistent with TCAB1 promoting telomerase assembly.
529

530 **Location and molecular mechanism of telomerase assembly**

531 The sub-cellular location and order in which telomerase RNP components associate with
532 TR in human cells have largely been unknown. It has been suggested that telomerase
533 assembly occurs in the DFC of the nucleolus (Lee et al., 2013) . While this study clearly
534 demonstrates that catalytically active telomerase can localize to the DFC of the nucleolus
535 (Lee et al., 2013), it fails to show that telomerase is assembled in the nucleolus. Results
536 by others have demonstrated that eliminating Cajal bodies does not impact telomerase

537 activity or telomere maintenance, suggesting that Cajal bodies are not necessary for
538 telomerase assembly (Chen et al., 2018, 2015; Vogan et al., 2016). Our single-molecule
539 live cell imaging of TERT demonstrates that TERT is almost exclusively localized to the
540 nucleoplasm. Since Cajal bodies are dispensable for telomerase assembly, and TERT is
541 largely excluded from the nucleolus, we believe telomerase assembly occurs in the
542 nucleoplasm. This model is further supported by our observation that expression of
543 LhTRmin, which lacks the binding sites for dyskerin and TCAB1 and therefore
544 accumulates in the nucleoplasm and is excluded from nucleoli in human cancer cells
545 (Vogan et al., 2016), rescues the telomerase assembly defect observed in the absence
546 of TCAB1. However, it is important to point out that we do observe a very small number
547 of TERT molecules that localize to nucleoli in control and TCAB1 knockout cells. These
548 static nucleolar TERT molecules require the presence of TR and therefore likely represent
549 TERT associated with TR. Unfortunately, we are unable to determine whether this
550 assembly of TERT and TR occurred in the nucleolus or prior to import of an assembled
551 telomerase RNP into the nucleolus.

552 TCAB1 could counteract TR accumulation in the nucleolus by two possible
553 mechanisms. Either TCAB1 could prevent the entry of TR into the nucleolus, increasing
554 the nucleoplasmic concentration of TR and the likelihood of assembly with TERT.
555 Alternatively, TCAB1 could extract telomerase assembled in the nucleolus by
556 accelerating the export of telomerase from the DFC. Because TCAB1 rarely enters the
557 nucleolus, we believe that it is unlikely that it contributes to the export of scaRNPs from
558 the nucleolus. In addition, if the presence of TCAB1 accelerated the dynamic exchange
559 of dyskerin-bound scaRNPs between the nucleolus and the nucleoplasm, we would

560 expect dyskerin to bind more tightly to the nucleolus in the absence of TCAB1. Instead,
561 our FRAP experiments demonstrate that the association of dyskerin with the nucleolus is
562 unchanged in the absence of TCAB1.

563 Altogether, our observations support our model that TCAB1 promotes telomerase
564 assembly by counteracting TR accumulation in the nucleolus to facilitate its assembly
565 with TERT in the nucleoplasm. Our analysis of the dynamics of nucleolar TR suggests
566 that it is tightly associated with the DFC when it is not bound by TCAB1. Since TCAB1
567 rarely enters the nucleolus, we believe the primary role of TCAB1 is to prevent the entry
568 of TR into the nucleolus. In the absence of TCAB1 the equilibrium of TR localization is
569 shifted towards the nucleolus, because re-entry is not inhibited by TCAB1 and the
570 dissociation of TR from the DFC is very slow. The resulting nucleolar accumulation of TR
571 effectively reduces the amount of TR available to assemble with TERT. Importantly, a
572 very small number of TERT molecules bound to TR can be imported and trapped in the
573 nucleolus, which would further decrease the amount of telomerase available to elongate
574 telomeres.

575

576 **Regulation of RNP assembly by nucleolar phase-separation**

577 In addition to the mechanistic insight into the role of TCAB1 in telomerase function, our
578 results also demonstrate that nucleolar phase separation can effectively regulate
579 telomerase RNP assembly in the nucleus of human cells. How RNA molecules are
580 specifically recruited into, excluded from, or expelled from non-membrane bound
581 organelles is a key unanswered question. One model suggests that gradual replacement
582 of non-specific, multivalent interactions of pre-ribosomal RNAs with nucleolar proteins

583 such as NPM1 and fibrillarin, with specific, high-affinity interactions with ribosomal
584 proteins leads to the ejection of mature ribosomal subunits from the nucleolus (Riback et
585 al., 2020). In this model a key driving force for the retention of RNA in the nucleolus is
586 regions of RNA not yet bound by ribosomal proteins, that are available to interact with
587 nucleolar proteins (Riback et al., 2020). By analogy, this model would explain why TR
588 bound by the H/ACA complex but not associated with TERT would be sequestered in the
589 nucleolus. Our experiments demonstrate that 60% of nucleolar TR is tightly associated
590 with the nucleolus while the remaining 40% can exchange with the nucleoplasm, which
591 closely corresponds to fraction of telomerase assembly observed in TCAB1 knock-out
592 cells. We believe that TR bound to TERT can exchange with the nucleoplasm, but TR not
593 associated with TERT remains trapped in the nucleolus. In addition to the interactions
594 formed by the H/ACA complex with nucleolar proteins and RNA, the regions of TR that
595 are bound by TERT in the context of telomerase (i.e. the pseudoknot, template, and
596 CR4/CR5) would be available to form non-specific, multivalent interactions with nucleolar
597 proteins to strengthen the association of TR with the nucleolus and prevent its release
598 when it is not associated with TERT.

599 TR is a unique among the scaRNAs, because it contains the additional domains
600 that associate with TERT. Most other box H/ACA scaRNAs are substantially shorter (<150
601 nucleotides) than TR (451 nucleotides), and do not contain large regions that are not
602 bound by proteins and could form non-specific interactions with nucleolar proteins. It is,
603 therefore, possible that in cells lacking TCAB1, TR is strongly retained in the nucleolus
604 while other scaRNAs are less tightly bound, because they lack additional interaction sites
605 with nucleolar proteins. Consistent with this hypothesis, we observe multiple populations

606 of dyskerin with distinct binding dynamics in nucleoli. The weakly bound population could
607 include dyskerin bound to scaRNAs, that are not retained in the nucleolus because their
608 RNA targets, which would provide an additional interaction site, are not present in
609 nucleoli. In contrast, dyskerin bound to snoRNAs would strongly associate with the
610 nucleolus, because they also bind to their target RNAs. This provides a potential
611 explanation for the phenotypes observed in patients with TCAB1 mutations that suffer
612 from dyskeratosis congenita. The patients have a clear deficiency in telomerase function
613 (Zhong et al., 2011), but no defects in splicing have been reported, which would be the
614 consequence of complete loss of scaRNA function and their critical role in spliceosome
615 maturation.

616 The mechanism by which TCAB1 binding leads to the exclusion of TR and other
617 scaRNA from the nucleolus remains a key unanswered question. TCAB1 interacts with a
618 very short sequence motif in TR, which is far removed from the TR regions that associate
619 with TERT (Ghanim et al., 2021). It is, therefore, unlikely that TCAB1 binding leads to
620 exclusion of TR from the nucleolus by reducing the number of non-specific, multivalent
621 interactions TR can form with nucleolar proteins. As outlined above, we believe that
622 TCAB1 prevents localization of scaRNAs to the nucleolus, rather than extracting
623 scaRNAs that are already localized to the DFC. One potential explanation is that TCAB1
624 counteracts scaRNA recruitment to the nucleolus by inhibiting the nucleolar localization
625 signals within dyskerin (Heiss et al., 1999). Dissecting the molecular mechanism by which
626 TCAB1 leads to exclusion of TR from the nucleolus in future studies will undoubtably shed
627 light on the fundamental principles RNP recruitment to non-membrane bound organelles
628 and its physiological role in cell biology.

629 **Acknowledgements**

630 We would like to thank members of the Schmidt lab and J. Nandakumar for discussions
631 and critical reading of the manuscript and Luke Lavis (HHMI Janelia Research Campus)
632 for providing HaloTag dyes. This work was supported by grants from the NIH (R00
633 GM120386, R01GM141354) to J.C.S.. J.C.S. was a Damon Runyon Dale F. Frey
634 Scientist supported (in part) by the Damon Runyon Cancer Research Foundation (DFS-
635 24-17). S.B.C. acknowledges sustained support from the Ernest & Piroska Major
636 Foundation.

637

638 **Author contributions**

639 B.M.K. carried out IF-FISH experiments, telomere length by Southern blot, cell cycle flow
640 cytometry and analysis, single molecule imaging, FRAP analysis, telomerase
641 purifications, cellular fractionations, analyzed telomerase assembly, generated mCherry-
642 and 3xFLAG-HaloTag-dyskerin plasmids, determined their sub-cellular localization, and
643 edited the manuscript. G.I.P. maintained cell lines, established TCAB1 and TR knock-out
644 cell lines and carried out IF-FISH experiments. K.A.-B. assisted in establishing the TR
645 knock-out cell line and carried out characterization of the TR knock-out cells. S.B.C.
646 purified and characterized the anti-TERT sheep antibody. L.H. and K.Y. characterized
647 TCAB1 knock-out clones using Southern blots. E.M.P. generated the cell lines expressing
648 3xMS2-TR. J.C.S. carried out all other experiments, designed the research, analyzed
649 data, and wrote the manuscript.

650

651 **Competing interests**

652 The authors declare no competing interests.

653 **Materials and Methods**

654 **Cell Lines and Tissue Culture**

655 All cell lines were based on HeLa-EM2-11ht (Weidenfeld et al., 2009) and were cultured
656 in Dulbecco's Modified Eagle Medium including L-glutamine (Gibco) supplemented with
657 10% fetal bovine serum, 100 units/ml penicillin and 100 µg/ml streptomycin at 37°C with
658 5% CO_2. Live cell imaging was carried out using CO_2 independent media supplemented
659 with 2 mM GlutaMAX (Life Technologies), 10% fetal bovine serum, 100 units/ml penicillin
660 and 100 µg/ml streptomycin at 37°C with 5% CO_2. For single-molecule imaging of
661 HaloTag-TERT cell were cultured in homemade imaging dishes made by gluing 22x22
662 mm Nexterion coverslips (170 ± 5 µm, Schott) onto the bottom of plastic 3.5 x 1.0 cm cell
663 culture dishes with a hole in the middle using an epoxy adhesive. Prior to chamber
664 assembly the coverslips were washed with 1 M KOH and 100% for 30 min each in a
665 sonicating water bath. To enrich for cells in S-phase for live cell imaging experiments,
666 cultures we treated with complete media including 2 mM thymidine for a minimum of 16
667 hours. Cells were released 2 hours prior to imaging by replacing the thymidine containing
668 media with fresh media without thymidine. Puromycin selection was carried out at a
669 concentration of 1 µg/ml.

670

671 **Plasmid Construction and Genome Editing**

672 All plasmids were generated by Gibson assembly (NEB) using standard protocols or by
673 inverse PCR. All plasmids will be made available on Addgene. All Cas9 and sgRNA
674 expression plasmids were based on pX330 (Cong et al., 2013). The homologous
675 recombination donor for the TR knock-out was generated by assembling the genomic

676 sequences immediately upstream and downstream (~500 bp each, gBlocks IDT) of the
677 TR sequence flanking a puromycin resistance cassette into HpaI linearized pFastBac.
678 The homologous recombination donor for the insertion of the 3xMS2-tag at the
679 endogenous was generated by cloning a left homology arm (418 bp upstream of the
680 *TERC* gene, gBlock IDT) followed by 3xMS2-TR and 100 bp of the genomic sequence
681 downstream of TR, followed by an SV40-promoter driven puromycin resistance marker,
682 and finally a right homology arm (473 bp, 101-573 bp downstream of the *TERC* gene,
683 gBlock IDT) into pFastBac. The sgRNA were designed to cut at the junction of the 3xMS2-
684 TR insert junctions and the PAM sites were mutated to not be present in the homologous
685 recombination donor plasmid, to assure the recombined allele was not cut by Cas9. The
686 lentiviral plasmids for expression of MCP-NeonGreen was generated by replacing the
687 sfGFP sequence in the pHAGE-UBC-MCP-sfGFP plasmid (a kind gift from Agnel Sfeir)
688 with the coding sequence for mNeonGreen. The lentivirus and cell lines expressing MCP-
689 mNeonGreen were generated as previously described (Querido et al., 2020). The
690 homologous recombination donor for the insertion of the 3xFLAG-HaloTag into the
691 *TCAB1* gene was generated by cloning the 3xFLAG-HaloTag sequence including a
692 SV40-promoter driven puromycin resistance marker flanked by LoxP-sites in between two
693 homology arms (500 bp up and downstream from the start codon, gBlocks IDT). The
694 3xFLAG-HaloTag-NLS plasmids was generated by adding a 3xFLAG-tag to a previously
695 described HaloTag-NLS plasmid (a kind gift from X. Darzacq and A. Hansen) (Hansen et
696 al., 2018). The 3xFLAG-HaloTag-dyskerin plasmid was generated by replacing TERT in
697 our previously described 3xFLAG-HaloTag-TERT expression plasmid with the dyskerin
698 coding sequence (Schmidt et al., 2016). The mCherry-dyskerin plasmid was generated

699 by replacing TERT in our previously described mCherry-TERT expression plasmid with
700 the dyskerin coding sequence (Schmidt et al., 2014). Unless otherwise stated,
701 transfections were carried out with Lipofectamine 2000 (Invitrogen) using the
702 manufacturer's instructions. For FRAP analysis of dyskerin $1x10^6$ HeLa cells were
703 transfected with 1 µg of 3xFLAG-HaloTag-dyskerin plasmid using the Lonza 4D-
704 Nucleofector with the SE Cell Line 4D-Nucleofector X kit (Cat. V4XC-1012) and program
705 CN-114. For single-molecule imaging of dyskerin 1 µg of a GFP-NPM1 plasmid was
706 included in addition to the 1 µg of 3xFLAG-HaloTag-dyskerin plasmid. GFP-NPM1 WT
707 was a gift from Xin Wang (Addgene plasmid #17578; http://n2t.net/addgene:17578;
708 RRID:Addgene_17578) (Wang et al., 2005). For single-molecule imaging of 3xFLAG-
709 HaloTag-NLS, 1 µg of a GFP-Nucleolin plasmid was included in addition to the 1 µg of
710 3xFLAG-HaloTag-NLS plasmid. The GFP-Nucleolin plasmid was a gift from Michael
711 Kastan (Addgene plasmid #28176; http://n2t.net/addgene:28176; RRID:
712 Addgene_28176) (Takagi et al., 2005). For FRAP analysis of nucleolar 3xMS2-TR 1 µg
713 of mTagBFP-Nucleus-7 was transfected into HeLa cells expressing 3xMS2-TR and MCP-
714 mNeonGreen. mTagBFP-Nucleus-7 was a gift from Michael Davidson (Addgene plasmid
715 # 55265 ; http://n2t.net/addgene:55265 ; RRID:Addgene_55265). TCAB1 was knocked-
716 out using a single sgRNA or two separate sgRNA and Cas9 encoding plasmids that were
717 transfected alongside a GFP-expressing plasmid. 24 hours after transfection single-cell
718 clones were sorted using the GFP signal. TCAB1 knock-out clones were screened by
719 PCR and confirmed by western blot, Southern Blotting of the *TCAB1* locus and
720 immunofluorescence imaging. TR was knocked out by transfecting two sgRNA plasmids
721 and a homologous recombination donor plasmid. 48 hours after transfection puromycin

722 selection was initiated and 1 week after the initiation of selection single-cell clones were
723 generated by dilution into 96-well plates. TR knock-out was confirmed using PCR and
724 Sanger sequencing, fluorescence *in situ* hybridization, and RT-qPCR.
725

726 **Immunofluorescence and Fluorescence *In Situ* Hybridization Imaging**

727 Fixed cell immunofluorescence imaging and fluorescence *in situ* hybridization was carried
728 out as previously described (Schmidt et al., 2014). Briefly, cells grown on coverslips were
729 fixed in PBS supplemented with 4% formaldehyde. When using the HaloTag for
730 fluorescence detection cells were incubated with 100 nM of JF646 HaloTag-ligand for 30
731 min prior to fixation. Unincorporated ligand was removed by 3 washes with complete
732 media followed by placing the cells back in the incubator for 10 min to let additional dye
733 leak out of the cells. mEOS3.2-TRF2 was detected using the intrinsic fluorescence of
734 green form of mEOS3.2. After removing the fixation solution using 2 PBS washes,
735 coverslips were transferred into aluminum foil covered humidity chambers with a parafilm
736 layer and rinsed with 1 ml of PBS with 0.2% Triton X-100. Cells were than incubated in
737 blocking buffer (PBS, 0.2% Triton X-100, 3% BSA) for 30 minutes, followed by incubation
738 with primary antibodies diluted in blocking buffer for 1 hour. All primary antibodies were
739 used at a concentration of 1 µg/ml. After three washes with PBS + 0.2% Triton X-100,
740 coverslips were incubated with secondary antibodies diluted in PBS + 0.2% Triton X-100
741 for 1 hour. All secondary antibodies were used at a concentration of 4 µg/ml. Cells were
742 washed three times PBS + 0.2% Triton X-100 prior to a second fixation with PBS + 4%
743 formaldehyde. In cases where nuclear staining was used, the first of the three washing
744 steps also included 0.1 µg/ml HOECHST. After the second fixation steps, coverslips were

745 dehydrated in three steps with ethanol (70%, 95%, 100%), re-hydrated in 2xSSC + 50%
746 formamide, blocked for 1 hour in hybridization buffer (100 mg/ml dextran sulfate, 0.125
747 mg/ml *E. coli* tRNA, 1 mg/ml nuclease free BSA, 0.5 mg/ml salmon sperm DNA, 1 mM
748 vanadyl ribonucleoside complexes, 50% formamide, 2xSSC) at 37°C, before incubating
749 the coverslips in hybridization buffer supplemented with three TR probes (30 ng per
750 coverslip,
751 /5Cy5/GCTGACATTTTTTGTTTGCTCTAGAATGAACGGTGGAAGGCGGCAGGCCGA
752 GGCTT,
753 /5Cy5/CTCCGTTCCTCTTCCTGCGGCCTGAAAGGCCTGAACCTCGCCCTCGCCCCC
754 GAGAG,
755 /5Cy5/ATGTGTGAGCCGAGTCCTGGGTGCACGTCCCACAGCTCAGGGAATCGCGC
756 CGCGCGC) overnight at 37°C. Probe sequences were previously described (Tomlinson
757 et al., 2006). After hybridization coverslips were washes twice for 30 minutes in 2xSSC +
758 50% formamide and then mounted on slides using ProLong Antifade Diamond mounting
759 media (Life Technologies). Microscopy was carried out using a DeltaVision Elite
760 microscope using a 60x PlanApo objective (1.42 NA) and a pco.edge sCMOS camera.
761 We acquired 20 Z-sections spaced by 0.2 μm, followed by image deconvolution and
762 maximum intensity projection of the sections using the DeltaVision Softworx software.
763

764 **Single-Molecule Live Cell Imaging**

765 Live cell single-molecule imaging was carried out on an Olympus IX83 inverted
766 microscope equipped with a 4-line cellTIRF illuminator (405 nm, 488 nm, 561 nm, 640 nm
767 lasers), an Excelitas X-Cite TURBO LED light source, a Olympus UAPO 100x TIRF

768 objective (1.49 NA), a CAIRN TwinCam beamsplitter, 2 Andor iXon 897 Ultra EMCCD
769 cameras or 2 Hamamatsu Orca BT Fusion cameras, a cellFRAP with a 100 mW 405 nm
770 laser, and a blacked-out environmental control enclosure. The microscope was operated
771 using the Olympus cellSense software. 3xFLAG-HaloTag-TERT was labeled for 2 min in
772 complete media supplemented with 100 nM JF646-HaloTag ligand (Grimm et al., 2015).
773 After removing the HaloTag-ligand with three washes in complete media, cells were
774 placed back in the incubator for 10 min to allow unincorporated dye to leak out of the
775 cells. Cells were then transferred into CO_2 independent media and put on the microscope
776 which was heated to 37°C. Single-molecule imaging was carried out at 50 or 100 frames
777 per second using highly inclined laminated optical sheet illumination (Tokunaga et al.,
778 2008). Movies were typically 20 seconds in length (2000 frames) and were followed by a
779 transmitted light acquisition to visualize overall cell morphology.For single-molecule
780 imaging of 3xFLAG-HaloTag-Dyskerin, cells were labeled with 100 pM of JFX650-
781 HaloTag Ligand (Grimm et al., 2020) for 1 min. Imaging was carried out at 100 frames
782 per second and images of GFP-NPM1 were taken before and after single-molecule
783 movies of dyskerin to assure the position of the nucleolus had not shifted.
784

785 **RT-qPCR**

786 RNA samples for RT-qPCR analysis were generated by using RNeasy Mini kits (Qiagen)
787 using ~2 million cells as starting material. Reverse transcription was carried out using
788 random hexamer primers and SuperScript III reverse transcriptase (Invitrogen) according
789 to the manufacturer's instructions. qPCR was carried out using the Maxima SYBR Green
790 qPCR master mix (Thermo Scientific) using primers for GAPDH and TR according to the

791 manufacturer's instructions. All qPCR reactions were carried out in triplicates and three
792 independent biological replicates were analyzed.
793
794 **Southern Blotting**
795 Southern blotting was carried out using standard protocols (Southern, 2006). Briefly,
796 genomic DNA generated by phenol-chloroform extraction after cell lysis using TE
797 supplemented with 0.5% SDS and 0.1 mg/ml Proteinase K, was digested with BamHI
798 (generating a 1394 bp fragment spanning exons 1-3 of the *TCAB1* locus) and separated
799 on a 0.8% agarose gel. The DNA was then transferred on a Hybond-N+ nylon membrane
800 using capillary transfer. The *TCAB1* locus was detected using radioactive probes (alpha-
801 ^{32}P-dCTP) generated by randomly primed DNA synthesis using an 800 bp PCR product
802 overlapping with the 1394 bp restriction fragment as a template and Klenow polymerase
803 (NEB). Telomeric restriction fragment analysis was carried out as previously described
804 (Nandakumar et al., 2012).
805
806 **Western Blotting**
807 Mini-PROTEAN TGX stain-free gels (Bio-Rad) were used for SDS-PAGE. Total protein
808 was detected using a ChemiDoc MP (Bio-Rad) after a 45 second UV activation. Western
809 transfer was carried out using the Trans-Blot Turbo transfer system (Bio-Rad) according
810 to the manufacturer's instructions using the mixed molecular weight transfer setting.
811 Immuno-blotting was carried out using standard protocols. The C-terminal TCAB1
812 antibody (Proteintech, 14761-1-AP) was used at a 1:2000 dilution, the N-terminal TCAB1
813 antibody (Novus Biologicals, NB100-68252) was used at a 1:1000 dilution, the TERT

814 antibody (Abcam, ab32020) was used at a 1:4000 dilution, the dyskerin antibody (Santa
815 Cruz Biotech, sc-373956) was used at a 1:200 dilution, the fibrillarin antibody was used
816 at a 1:2000 dilution (Novus Biologicals, NB300-269), and the lamin B1 antibody was used
817 a 1:2000 dilution. Secondary antibodies were used at a 1:5000 dilution.
818
819 **Northern Blotting**
820 RNA was extracted from cell lysates, cellular fractions, and purified telomerase samples
821 using the RNeasy Mini kit (Qiagen) and eluted in 30 ul of RNase free water. Purified
822 telomerase samples were supplemented with 10 ng of a loading and recovery control
823 prior to RNA extraction (*in vitro* transcribed TR 34-328). 15 ul of eluted RNA was mixed
824 with 15 ul of 2x formamide loading buffer (0.1XTBE, 25 mM EDTA, 0.1% bromophenol
825 blue, 0.1% xylene cyanol, 93% formamide) and heated to 60 °C for 5 min. Samples were
826 separated on a 6% TBE, 7M Urea, polyacrylamide gel (Life Technologies), and
827 transferred to a Hybond N+ membrane (Cytiva) using a wet-blotting apparatus in 1x TBE
828 for 2 hours at 0.5 A of constant current in the cold room. After transfer, membranes were
829 UV-crosslinked, and pre-hybridized in Church buffer for 2 hours at 50 °C. Three DNA
830 oligos complementary to TR (GACTCGCTCCGTTCCTCTTC,
831 GCTCTAGAATGAACGGTGGAA, CCTGAAAGGCCTGAACCTC,
832 CGCCTACGCCCTTCTCAGT, ATGTGTGAGCCGAGTCCTG), 7SL
833 (GCGGACACCCGATCGGCATAGC), U3
834 (GCCGGCTTCACGCTCAGGAGAAAACGCTACCTCTCTTCCTCGTGG), and 7SK
835 (GTGTCTGGAGTCTTGGAAGC) were radioactively labeled using T4 PNK (NEB) and
836 ~$10x10^6$ cpm of each probe were added to the membrane. Hybridization was carried out

837 at 50 °C overnight. Membranes were washed three times with 2xSSC, 0.1% SDS prior to
838 exposure to a storage phosphorescence screen (Cytiva) which was then imaged on an
839 Amersham Typhoon IP phosphoimager (Cytiva).
840

841 **Telomerase Expression and Purification**

842 Cell lines were transfected in 15-cm tissue culture plates at ~90% confluency (~25-30x10^6
843 cells) using 7.5 µg of TERT plasmid, 30 µg of TR plasmid and 75 µl of Lipofectamine 2000
844 in 1875 ul of Opti-MEM (Cristofari and Lingner, 2006). The same amounts were used in
845 transfecting LhTRmin (Vogan et al., 2016) or pBS U3-hTR-500 (Addgene plasmid #
846 28170 ; http://n2t.net/addgene:28170 ; RRID:Addgene_28170) (Fu and Collins, 2003)
847 plasmids, which were generously gifted by Kathleen Collins . Transfected cells were split
848 to three 15 cm dishes 24 hours after transfection. 48 hours after transfection cells were
849 counted, harvested, and snap frozen in liquid nitrogen. Cells were lysed in 1 ml of CHAPS
850 lysis buffer supplemented with 5 µl of RiboLock RNase inhibitor (10 mM TRIS pH 7.5, 1
851 mM $MgCl_2$, 1 mM EGTA pH 8.0, 0.5% CHAPS, 10% glycerol) per 100x10^6 cells and
852 rotated at 4 °C for 30 min. Lysates were cleared in a table-top centrifuge at 21,000xg for
853 15 min at 4 °C. Identical cell equivalents were used for all samples. 45 µg of anti-TERT
854 antibody was added per ml of cleared lysate and samples were rotated for 1 hour at 4 °C.
855 Lysates were then added to 100 µl of protein G agarose and rotated for 1 hour at 4 °C.
856 The resin was spun down at 1000xg and washed four times with 1 ml of Buffer W (20 mM
857 HEPES pH 7.9, 300 mM KCl, 2 mM $MgCl_2$, 1 mM EDTA, 1 mM DTT, 1 mM PMSF, 0.1%
858 Triton X-100, 10% glycerol). TERT was eluted in 100 µl of Buffer W supplemented with 5
859 µl of 1 mM TERT peptide by rotating for 30 min at room temperature.

860

861 **Telomerase Activity Assays**

862 Telomerase assays were carried out in 20 µl of reaction buffer (50 mM TRIS pH 8.0, 150
863 mM KCl, 1 mM MgCl2, 2 mM DTT, 100 nM TTAGGGTTAGGGTTAGG oligo, 10 µM dATP,
864 10 µM dGTP, 10 µM dTTP, 0.165 µM dGTP [α-32P] 3000 Ci/mmol) including 2 µl of
865 purified telomerase for 1 hour at 30 °C. Telomerase was incubated with the substrate
866 oligo for 15 min at room temperature, prior to initiating the reaction by addition of dNTPs.
867 Reactions were stopped by adding 100 µl of 3.6 M of ammonium acetate supplemented
868 with 20 µg of glycogen and 32P 5'-end labeled loading control oligos
869 (TTAGGGTTAGGGTTAGGG, TTAGGGTTAGGGTTAG). Reaction products were
870 precipitated using 500 µl of ice-cold ethanol and stored at -20 °C over-night. Reaction
871 products were spun down in a table-top centrifuge at max speed for 30 min at 4 °C,
872 washed with 500 µl of 70% ethanol, and spun down again speed for 30 min at 4 °C. The
873 70% ethanol was decanted, and the reaction products were dried in an Eppendorf
874 vacuum concentrator at 45 °C. Reaction products were resuspended in 20 µl of loading
875 buffer (0.05XTBE, 25 mM EDTA, 0.05% bromophenol blue, 0.05% xylene cyanol, 46.5%
876 formamide) and incubated at 95 °C for 5 min. 10 µl of each sample was separated on a
877 12% polyacrylamide, 7 M urea sequencing gel pre-run for 45 min at 90W. Gels were dried
878 and exposed to a storage phosphorescence screen (Cytiva) and imaged on an
879 Amersham Typhoon IP phosphoimager (Cytiva).

880

881 **Nucleolar Isolation**

882 Cellular fractionation was carried out using a as previously described (Lam and Lamond,
883 2006). All procedures were carried out on ice and centrifugations at 4 °C. Approximately
884 $1x10^6$ million cells were harvested by trypsinization, washed with PBS, followed
885 by incubation in a hypotonic buffer (10 mM HEPES pH 7.9, 10 mM KCl, 1.5 mM $MgCl_2$,
886 0.5 mM DTT) to swell the cells. A small fraction of the swollen cells was collected as input
887 sample. Swollen cells were then ruptured using pre-cooled dounce homogenizer and the
888 tight pestle (VWR Cat. 62400-595). The ruptured cells were centrifuged at 218xg for 5
889 min to pellet nuclei. Nuclei where then resuspended in buffer S1 (0.25 M sucrose, 10 mM
890 $MgCl_2$), layered on top of buffer S2 (0.35 M sucrose, 0.5 mM $MgCl_2$) in a 15 ml conical
891 tube, and centrifuged at 1430xg in a swinging bucket rotor for 5 min to further purify nuclei.
892 Nuclei were resuspended in buffer S2 and sonicated on ice for 10 seconds at 30% power
893 (Fisherbrand Model 505, 500W). The sonicated nuclei were then layered on top of buffer
894 S3 (0.88 M sucrose, 0.5 mM $MgCl_2$) and centrifuged at 3000xg in a swinging bucket rotor
895 for 5 min to further purify nucleoli. The nucleolar pellet was suspended in buffer S2 and
896 centrifuged a final time at 1430xg to yield a highly purified nucleolar pellet, which was
897 resuspended in buffer S2. Equal fractions of input, cytoplasm, nuclei, nucleoplasm, and
898 nucleoli samples were collected and analyzed by western and northern blots. To test the
899 impact of salt concentration on the integrity of nucleoli, nuclei ruptured by sonication were
900 mixed 1:1 with buffer S2 containing 40 mM HEPES pH7.9 with and without 715 mM KCl,
901 prior layering the solution on top of buffer S3.
902
903 **Cell Synchronization and Flow Cytometry**

904 Cell lines in 15-cm tissue culture plates at a 70% confluency were blocked with 2 mM
905 thymidine then released from thymidine after 24 hours and harvested at four time points
906 post release: 0, 4, 8 hours. Along with each synchronization, asynchronous population
907 was also harvested. Cells were harvested using PBS supplemented with 5 mM EDTA
908 then fixed with ethanol, stained with propidium iodide for DNA content, and finally filtered
909 to generate a single cell suspension. Stained samples were run through BD Accuri C6
910 cytometer and cell-cycle distributions were analyzed on OriginLab.
911

912 **Single-Particle Tracking**

913 Single-particle tracking was carried out in MATLAB 2019a using a batch parallel-
914 processing version of SLIMfast modified to allow the input of TIFF files (kindly provided
915 by Xavier Darzacq and Anders Hansen) (Hansen et al., 2018), an implementation of the
916 Multiple-Target-Tracing algorithm (Sergé et al., 2008), with the following settings:
917 Exposure Time = 10 ms, NA = 1.49, Pixel Size = 0.16 μm, Emission Wavelength = 664
918 nm, D_{max} = 5 $\mu m^2/s$, Number of gaps allowed = 2, Localization Error = 10^{-5}, Deflation
919 Loops = 0. Diffusion coefficients and the fraction of molecules in each distinct particle
920 population were determined using the MATLAB version of the Spot-On tool (kindly
921 provided by Xavier Darzacq and Anders Hansen) (Hansen et al., 2018) with the following
922 settings: TimeGap = 10 ms or 20 ms, dZ = 0.700 μm, GapsAllowed = 2, TimePoints = 8,
923 JumpsToConsider = 4, BinWidth = 0.01 μm, PDF-fitting, D_Free1_3State = [1 25],
924 D_Free2_3State = [0.1 1], D_Bound_3State = [0.0001 0.1]. For all experiments we carried
925 out 3 independent biological replicates with at least 15 cells for each cell line. The

926 statistical significance of differences in particle fractions and diffusion coefficients were
927 assessed using a two-tailed T-Test.
928 For the analysis of dyskerin trajectories a mask of the nucleolus was generated manually
929 using the threshold function in FIJI. Dyskerin trajectories whose coordinates overlapped
930 with the nucleolar mask for a single frame were designated as nucleolar trajectories. The
931 remaining trajectories were designated nuclear trajectories. All data sets were analyzed
932 using Spot-On as described above.
933
934 **Fluorescence recovery after photobleaching**
935 Fluorescence recovery experiments (FRAP) we carried out using the same Olympus
936 microscope used for single-molecule imaging. Cells were stained for 10 min with 100 nM
937 JFX650-HaloTag ligand in complete media. After removing the HaloTag-ligand with three
938 washes in complete media, cells were placed back in the incubator for 10 min to allow
939 unincorporated dye to leak out of the cells. Cells were then transferred into CO_2
940 independent media and put on the microscope which was heated to 37°C. We identified
941 cells with two clearly visible nucleoli and bleached one of them by placing three diffraction
942 limited bleach spots within the nucleolar 3xFLAG-HaloTag-dyskerin signal. Each spot was
943 bleached for 100 ms at 50% laser power, which lead to complete loss of the fluorescence
944 within the nucleolus. Cells were imaged prior to and after bleaching at 1 frame per second
945 using the Excelitas X-cite TURBO LED light source and the 100x objective.
946 Photobleaching due to LED exposure was negligible. To quantify FRAP we first drift
947 corrected the movie using NanoJ (Laine et al., 2019), we then placed a region of interest
948 (ROI) within the nucleolus and quantified mean intensity within the ROI over time.

949 Background signal was determined in an area of the field of view that was not covered by
950 a cell and subtracted from the nucleolar ROI. In addition, the mean fluorescence after the
951 bleaching pulse was divided by the fraction of total cellular fluorescence remaining after
952 the bleaching pulse. Because the laser pulse bleaches a significant amount of total
953 cellular fluorescence (typically 20-40%), this normalization is critical to determine the
954 maximal amount of fluorescence recovery possible. For example, if 30% of total cellular
955 fluorescence is lost due to the bleaching pulse, the maximal fraction of pre-bleach
956 fluorescence than can theoretically be recovered is 70%. The recovery data was then fit
957 using a single exponential function ($1-A*e^{-kt}+C$), where k corresponds to the rate constant
958 and C to the fraction of the initial signal that is not recovered (i.e. the static fraction).
959 For the FRAP analysis of nucleolar 3xMS2-TR bound by MCP-mNeonGreen cells were
960 imaged on a Olympus SpinSR spinning disk confocal microscope equipped with a
961 cellFRAP unit and a Hamamatsu ORCA Fusion BT camera. 3xMS2 TR clearly localized
962 to the DFC of the nucleolus marked by mTagBFP-Nucleus-7 was bleached using the 405
963 nm laser line and recovery of the MCP-mNeonGreen was imaged every second using the
964 488 nm laser line. Data analysis was varied out as described above.
965

966 **Quantification of Fixed Cell Imaging**

967 For the quantification of cellular TR distribution in control and TCAB1 knock-out cells we
968 assigned cells into one of three categories: cells with TR only at telomeres, cells with TR
969 only in nucleoli, and cells with TR at telomeres and in nucleoli. We carried out 3
970 independent biological replicates and counted a minimum of 100 cells for control and
971 TCAB1 knock-out cells.

972

973 **Quantification of RT-qPCR data**

974 RT-qPCR experiments were carried out in triplicate and the TR Ct value was normalized
975 to the GAPDG Ct value. The mean ΔCt (Ct of TR – Ct of GAPDH) value from three
976 independent experiments and the corresponding standard deviation were plotted.

977

978 **Quantification of Western Blots, Northern Blots, and Telomerase Activity Assays**

979 Gel images from western Blots, northern Blots, and telomerase activity assays were
980 analyzed using ImageQuant TL 8.2. To quantify TR levels in Northern blots the TR band
981 intensity was normalized to the loading and recovery control signal added to the RNA
982 sample prior to RNA purification. To quantify telomerase activity, the whole lane intensity
983 starting at repeat 1 was determined and divided by the sum of the loading control signals.
984 Telomerase processivity was calculated by dividing product intensity > 7 repeats by the
985 total signal in the respective lane. The statistical significance of the observed differences
986 was calculated using a two-tailed T-test using a minimum of three biological replicates.
987 Each biological replicate (independent telomerase expression and purification) was
988 analyzed in technical triplicate.

989

990

991 **References**

992

993 Angrisani A, Vicidomini R, Turano M, Furia M. 2014. Human dyskerin: beyond
994 telomeres. *Biol Chem* **395**:593–610. doi:10.1515/hsz-2013-0287

995 Armanios M, Blackburn EH. 2012. The telomere syndromes. *Nat Rev Genet* **13**:693
996 704. doi:10.1038/nrg3246

997 Chen L, Roake CM, Freund A, Batista PJ, Tian S, Yin YA, Gajera CR, Lin S, Lee B,
998 Pech MF, Venteicher AS, Das R, Chang HY, Artandi SE. 2018. An Activity Switch in
999 Human Telomerase Based on RNA Conformation and Shaped by TCAB1. *Cell* **174**.
1000 doi:10.1016/j.cell.2018.04.039

1001 Chen Y, Deng Z, Jiang S, Hu Q, Liu H, Songyang Z, Ma W, Chen S, Zhao Y. 2015.
1002 Human cells lacking coilin and Cajal bodies are proficient in telomerase assembly,
1003 trafficking and telomere maintenance. *Nucleic Acids Res* **43**:385–395.
1004 doi:10.1093/nar/gku1277

1005 Cohen SB, Graham ME, Lovrecz GO, Bache N, Robinson PJ, Reddel RR. 2007. Protein
1006 Composition of Catalytically Active Human Telomerase from Immortal Cells. *Science*
1007 **315**:1850–1853. doi:10.1126/science.1138596

1008 Cong L, Ran FA, Cox D, Lin S, Barretto R, Habib N, Hsu PD, Wu X, Jiang W, Marraffini
1009 LA, Zhang F. 2013. Multiplex Genome Engineering Using CRISPR/Cas Systems.
1010 *Science* **339**:819–823. doi:10.1126/science.1231143

1011 Cristofari G, Lingner J. 2006. Telomere length homeostasis requires that telomerase
1012 levels are limiting. *Embo J* **25**:565 574. doi:10.1038/sj.emboj.7600952

1013 Feric M, Vaidya N, Harmon TS, Mitrea DM, Zhu L, Richardson TM, Kriwacki RW, Pappu
1014 RV, Brangwynne CP. 2016. Coexisting Liquid Phases Underlie Nucleolar
1015 Subcompartments. *Cell* **165**:1686 1697. doi:10.1016/j.cell.2016.04.047

1016 Freund A, Zhong FL, Venteicher AS, Meng Z, Veenstra TD, Frydman J, Artandi SE.
1017 2014. Proteostatic Control of Telomerase Function through TRiC-Mediated Folding of
1018 TCAB1. *Cell* **159**:1389 1403. doi:10.1016/j.cell.2014.10.059

1019 Fu D, Collins K. 2003. Distinct biogenesis pathways for human telomerase RNA and
1020 H/ACA small nucleolar RNAs. *Mol Cell* **11**:1361 1372. doi:10.1016/s1097-
1021 2765(03)00196-5

1022 Gallardo F, Olivier C, Dandjinou AT, Wellinger RJ, Chartrand P. 2008. TLC1 RNA
1023 nucleo-cytoplasmic trafficking links telomerase biogenesis to its recruitment to
1024 telomeres. *Embo J* **27**:748 757. doi:10.1038/emboj.2008.21

1025 Ghanim GE, Fountain AJ, Roon A-MM van, Rangan R, Das R, Collins K, Nguyen THD.
1026 2021. Structure of human telomerase holoenzyme with bound telomeric DNA. *Nature*
1027 1–5. doi:10.1038/s41586-021-03415-4

1028 Grimm JB, English BP, Chen J, Slaughter JP, Zhang Z, Revyakin A, Patel R, Macklin
1029 JJ, Normanno D, Singer RH, Lionnet T, Lavis LD. 2015. A general method to improve
1030 fluorophores for live-cell and single-molecule microscopy. *Nat Methods* **12**:244 50–3
1031 p following 250. doi:10.1038/nmeth.3256

1032 Grimm JB, Xie L, Casler JC, Patel R, Tkachuk AN, Choi H, Lippincott-Schwartz J,
1033 Brown TA, Glick BS, Liu Z, Lavis LD. 2020. Deuteration improves small-molecule
1034 fluorophores. *Biorxiv* 2020.08.17.250027. doi:10.1101/2020.08.17.250027

1035 Hansen AS, Woringer M, Grimm JB, Lavis LD, Tjian R, Darzacq X. 2018. Robust
1036 model-based analysis of single-particle tracking experiments with Spot-On. *Elife* **7**.
1037 doi:10.7554/elife.33125

1038 Heiss NS, Girod A, Salowsky R, Wiemann S, Pepperkok R, Poustka A. 1999. Dyskerin
1039 Localizes to the Nucleolus and Its Mislocalization Is Unlikely to Play a Role in the
1040 Pathogenesis of Dyskeratosis Congenita. *Hum Mol Genet* **8**:2515–2524.
1041 doi:10.1093/hmg/8.13.2515

1042 Hyman AA, Weber CA, Jülicher F. 2014. Liquid-Liquid Phase Separation in Biology.
1043 *Annu Rev Cell Dev Bi* **30**:39–58. doi:10.1146/annurev-cellbio-100913-013325

1044 Jády BE, Bertrand E, Kiss T. 2004. Human telomerase RNA and box H/ACA scaRNAs
1045 share a common Cajal body–specific localization signal. *J Cell Biology* **164**:647–652.
1046 doi:10.1083/jcb.200310138

1047 Laine RF, Tosheva KL, Gustafsson N, Gray RDM, Almada P, Albrecht D, Risa GT,
1048 Hurtig F, Linds A-C, Baum B, Mercer J, Leterrier C, Pereira PM, Culley S, Henriques
1049 R. 2019. NanoJ: a high-performance open-source super-resolution microscopy
1050 toolbox. *J Phys D Appl Phys* **52**:163001. doi:10.1088/1361-6463/ab0261

1051 Lam YW, Lamond AI. 2006. Cell Biology (Third Edition). *Part Organelles Cell Struct*
1052 *Sect 1isolation Plasma Membr Organelles Cell Struct Sect 1 Isol Plasma Membr*
1053 *Organelles Cell Struct* 103–107. doi:10.1016/b978-012164730-8/50087-3

1054 Laprade H, Querido E, Smith MJ, Guérit D, Crimmins H, Conomos D, Pourret E,
1055 Chartrand P, Sfeir A. 2020. Single-Molecule Imaging of Telomerase RNA Reveals a
1056 Recruitment-Retention Model for Telomere Elongation. *Mol Cell*.
1057 doi:10.1016/j.molcel.2020.05.005

1058 Lee JH, Lee YS, Jeong SA, Khadka P, Roth J, Chung IK. 2013. Catalytically active
1059 telomerase holoenzyme is assembled in the dense fibrillar component of the

1060 nucleolus during S phase. *Histochem Cell Biol* **141**:137–52. doi:10.1007/s00418-013-
1061 1166-x

1062 Mitrea DM, Kriwacki RW. 2016. Phase separation in biology; functional organization of a
1063 higher order. *Cell Commun Signal Ccs* **14**:1. doi:10.1186/s12964-015-0125-7

1064 Nagpal N, Wang J, Zeng J, Lo E, Moon DH, Luk K, Braun RO, Burroughs LM, Keel SB,
1065 Reilly C, Lindsley RC, Wolfe SA, Tai AK, Cahan P, Bauer DE, Fong YW, Agarwal S.
1066 2020. Small-Molecule PAPD5 Inhibitors Restore Telomerase Activity in Patient Stem
1067 Cells. *Cell Stem Cell* **26**:896-909.e8. doi:10.1016/j.stem.2020.03.016

1068 Nandakumar J, Bell CF, Weidenfeld I, Zaug AJ, Leinwand LA, Cech TR. 2012. The TEL
1069 patch of telomere protein TPP1 mediates telomerase recruitment and processivity.
1070 *Nature* **492**:285 289. doi:10.1038/nature11648

1071 Nandakumar J, Cech TR. 2013. Finding the end: recruitment of telomerase to
1072 telomeres. *Nat Rev Mol Cell Bio* **14**. doi:10.1038/nrm3505

1073 Querido E, Sfeir A, Chartrand P. 2020. Imaging of Telomerase RNA by Single-Molecule
1074 Inexpensive FISH Combined with Immunofluorescence. *Star Protoc* **1**:100104.
1075 doi:10.1016/j.xpro.2020.100104

1076 Riback JA, Zhu L, Ferrolino MC, Tolbert M, Mitrea DM, Sanders DW, Wei M-T, Kriwacki
1077 RW, Brangwynne CP. 2020. Composition-dependent thermodynamics of intracellular
1078 phase separation. *Nature* **581**:209–214. doi:10.1038/s41586-020-2256-2

1079 Schmidt JC, Cech TR. 2015. Human telomerase: biogenesis, trafficking, recruitment,
1080 and activation. *Gene Dev* **29**:1095 1105. doi:10.1101/gad.263863.115

1081 Schmidt JC, Dalby AB, Cech TR. 2014. Identification of human TERT elements
1082 necessary for telomerase recruitment to telomeres. *Elife* **3**:e03563.
1083 doi:10.7554/elife.03563

1084 Schmidt JC, Zaug AJ, Cech TR. 2016. Live Cell Imaging Reveals the Dynamics of
1085 Telomerase Recruitment to Telomeres. *Cell* **166**:1188 1197.e9.
1086 doi:10.1016/j.cell.2016.07.033

1087 Schmidt JC, Zaug AJ, Kufer R, Cech TR. 2018. Dynamics of human telomerase
1088 recruitment depend on template-telomere base pairing. *Mol Biol Cell* **29**:869 880.
1089 doi:10.1091/mbc.e17-11-0637

1090 Sergé A, Bertaux N, Rigneault H, Marguet D. 2008. Dynamic multiple-target tracing to
1091 probe spatiotemporal cartography of cell membranes. *Nat Methods* **5**:687 694.
1092 doi:10.1038/nmeth.1233

1093 Shukla S, Jeong H-C, Sturgeon CM, Parker R, Batista LFZ. 2020. Chemical inhibition of
1094 PAPD5/7 rescues telomerase function and hematopoiesis in dyskeratosis congenita.
1095 *Blood Adv* **4**:2717–2722. doi:10.1182/bloodadvances.2020001848

1096 Shukla S, Schmidt JC, Goldfarb KC, Cech TR, Parker R. 2016. Inhibition of telomerase
1097 RNA decay rescues telomerase deficiency caused by dyskerin or PARN defects. *Nat*
1098 *Struct Mol Biol* **23**:286 292. doi:10.1038/nsmb.3184

1099 Southern E. 2006. Southern blotting. *Nat Protoc* **1**:518–525. doi:10.1038/nprot.2006.73

1100 Stern JL, Zyner KG, Pickett HA, Cohen SB, Bryan TM. 2012. Telomerase Recruitment
1101 Requires both TCAB1 and Cajal Bodies Independently. *Mol Cell Biol* **32**:2384–2395.
1102 doi:10.1128/mcb.00379-12

1103 Stewart SA, Weinberg RA. 2006. Telomeres: Cancer to Human Aging. *Annu Rev Cell*
1104 *Dev Bi* **22**:531–557. doi:10.1146/annurev.cellbio.22.010305.104518

1105 Stuart BD, Choi J, Zaidi S, Xing C, Holohan B, Chen R, Choi M, Dharwadkar P, Torres
1106 F, Girod CE, Weissler J, Fitzgerald J, Kershaw C, Klesney-Tait J, Mageto Y, Shay
1107 JW, Ji W, Bilguvar K, Mane S, Lifton RP, Garcia CK. 2015. Exome sequencing links
1108 mutations in PARN and RTEL1 with familial pulmonary fibrosis and telomere
1109 shortening. *Nat Genet* **47**:512 517. doi:10.1038/ng.3278

1110 Takagi M, Absalon MJ, McLure KG, Kastan MB. 2005. Regulation of p53 translation and
1111 induction after DNA damage by ribosomal protein L26 and nucleolin. *Cell* **123**:49 63.
1112 doi:10.1016/j.cell.2005.07.034

1113 Tokunaga M, Imamoto N, Sakata-Sogawa K. 2008. Highly inclined thin illumination
1114 enables clear single-molecule imaging in cells. *Nat Methods* **5**:159 161.
1115 doi:10.1038/nmeth1171

1116 Tomlinson RL, Ziegler TD, Supakorndej T, Terns RM, Terns MP. 2006. Cell cycle-
1117 regulated trafficking of human telomerase to telomeres. *Mol Biol Cell* **17**:955 965.
1118 doi:10.1091/mbc.e05-09-0903

1119 Tseng C-K, Wang H-F, Burns AM, Schroeder MR, Gaspari M, Baumann P. 2015.
1120 Human Telomerase RNA Processing and Quality Control. *Cell Reports* **13**:2232–
1121 2243. doi:10.1016/j.celrep.2015.10.075

1122 Tummala H, Walne A, Collopy L, Cardoso S, Fuente J de la, Lawson S, Powell J,
1123 Cooper N, Foster A, Mohammed S, Plagnol V, Vulliamy T, Dokal I. 2015. Poly(A)-
1124 specific ribonuclease deficiency impacts telomere biology and causes dyskeratosis
1125 congenita. *J Clin Invest* **125**:2151–2160. doi:10.1172/jci78963

1126 Tycowski KT, Shu M-D, Kukoyi A, Steitz JA. 2009. A conserved WD40 protein binds the
1127 Cajal body localization signal of scaRNP particles. *Mol Cell* **34**:47 57.
1128 doi:10.1016/j.molcel.2009.02.020

1129 Venteicher AS, Abreu EB, Meng Z, McCann KE, Terns RM, Veenstra TD, Terns MP,
1130 Artandi SE. 2009. A human telomerase holoenzyme protein required for Cajal body
1131 localization and telomere synthesis. *Science* **323**:644 648.
1132 doi:10.1126/science.1165357

1133 Vogan JM, Zhang X, Youmans DT, Regalado SG, Johnson JZ, Hockemeyer D, Collins
1134 K. 2016. Minimized human telomerase maintains telomeres and resolves
1135 endogenous roles of H/ACA proteins, TCAB1, and Cajal bodies. *Elife* **5**:693.
1136 doi:10.7554/elife.18221

1137 Wang W, Budhu A, Forgues M, Wang XW. 2005. Temporal and spatial control of
1138 nucleophosmin by the Ran–Crm1 complex in centrosome duplication. *Nat Cell Biol*
1139 **7**:823–830. doi:10.1038/ncb1282

1140 Weidenfeld I, Gossen M, Löw R, Kentner D, Berger S, Görlich D, Bartsch D, Bujard H,
1141 Schönig K. 2009. Inducible expression of coding and inhibitory RNAs from
1142 retargetable genomic loci. *Nucleic Acids Res* **37**:e50. doi:10.1093/nar/gkp108

1143 Wu RA, Upton HE, Vogan JM, Collins K. 2017. Telomerase Mechanism of Telomere
1144 Synthesis. *Annu Rev Biochem* **86**:439 460. doi:10.1146/annurev-biochem-061516-
1145 045019

1146 Yao R-W, Xu G, Wang Ying, Shan L, Luan P-F, Wang Yang, Wu M, Yang L-Z, Xing Y-
1147 H, Yang L, Chen L-L. 2019. Nascent Pre-rRNA Sorting via Phase Separation Drives
1148 the Assembly of Dense Fibrillar Components in the Human Nucleolus. *Mol Cell*
1149 **76**:767-783.e11. doi:10.1016/j.molcel.2019.08.014

1150 Zhong F, Savage SA, Shkreli M, Giri N, Jessop L, Myers T, Chen R, Alter BP, Artandi
1151 SE. 2011. Disruption of telomerase trafficking by TCAB1 mutation causes
1152 dyskeratosis congenita. *Gene Dev* **25**:11–16. doi:10.1101/gad.2006411

1153

1154

Supplementary Information

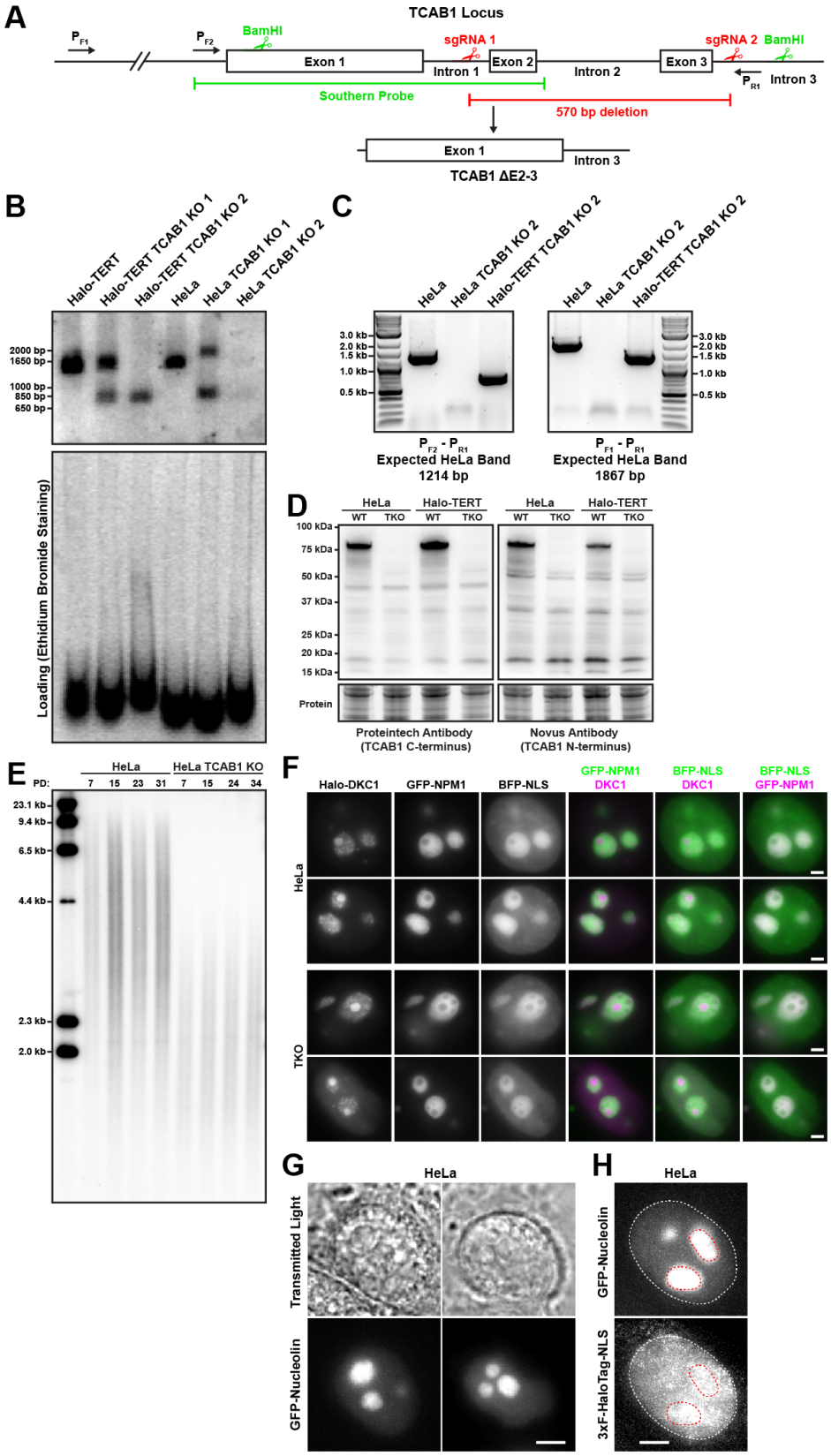

1157 **Supplementary Figure 1. (A)** Strategy to knock-out TCAB1 using Cas9 and two sgRNAs targeting
1158 introns 1 and 3. **(B)** Southern blot of genomic DNA digested with BamHI from parental cells and TCAB1
1159 knock-out clones using a probes generated from a PCR product of the TCAB1 gene indicated in **(A)**
1160 demonstrating the expected truncation of the *TCAB1* gene in Halo-TERT TCAB1 KO 2. HeLa TCAB1 KO
1161 2 carries larger deletions completely removing exons 1 and 2 from the *TCAB1* gene. **(C)** PCR using
1162 primers indicated in **(A)** of genomic DNA from parental cells and TCAB1 knock-out clones confirming the
1163 deletion of critical regions of the *TCAB1* gene show in **(B)**. **(D)** Western blots demonstrating the absence
1164 of TCAB1 protein in TCAB1 knock-out cell lines generated in HeLa and Halo-TERT cells lines using two
1165 antibodies targeting the N-terminus and C-terminus of TCAB1. **(E)** Telomere length analysis by Southern
1166 blot of telomeric restriction fragments, indicating that telomeres in TCAB1 knock-out cells are short but
1167 stable in length. **(G)** Images of HeLa cells transiently expressing GFP-nucleolin to mark nucleoli. The
1168 GFP-nucleolin signal overlaps with circular shapes visible under transmitted light illumination (scale bar =
1169 2 μm). **(H)** Images of HeLa cells transiently expressing GFP-nucleolin and 3xFLAG-HaloTag-NLS labeled
1170 with JF646. The 3xFLAG-HaloTag-NLS signal (maximum intensity projection of 1000 frames of a single-
1171 molecule imaging movie) clearly overlaps with the GFP-nucleolin signal (red dashed outline),
1172 demonstrating that 3xFLAG-HaloTag-NLS can enter the nucleolus (scale bar = 2 μm).
1173
1174

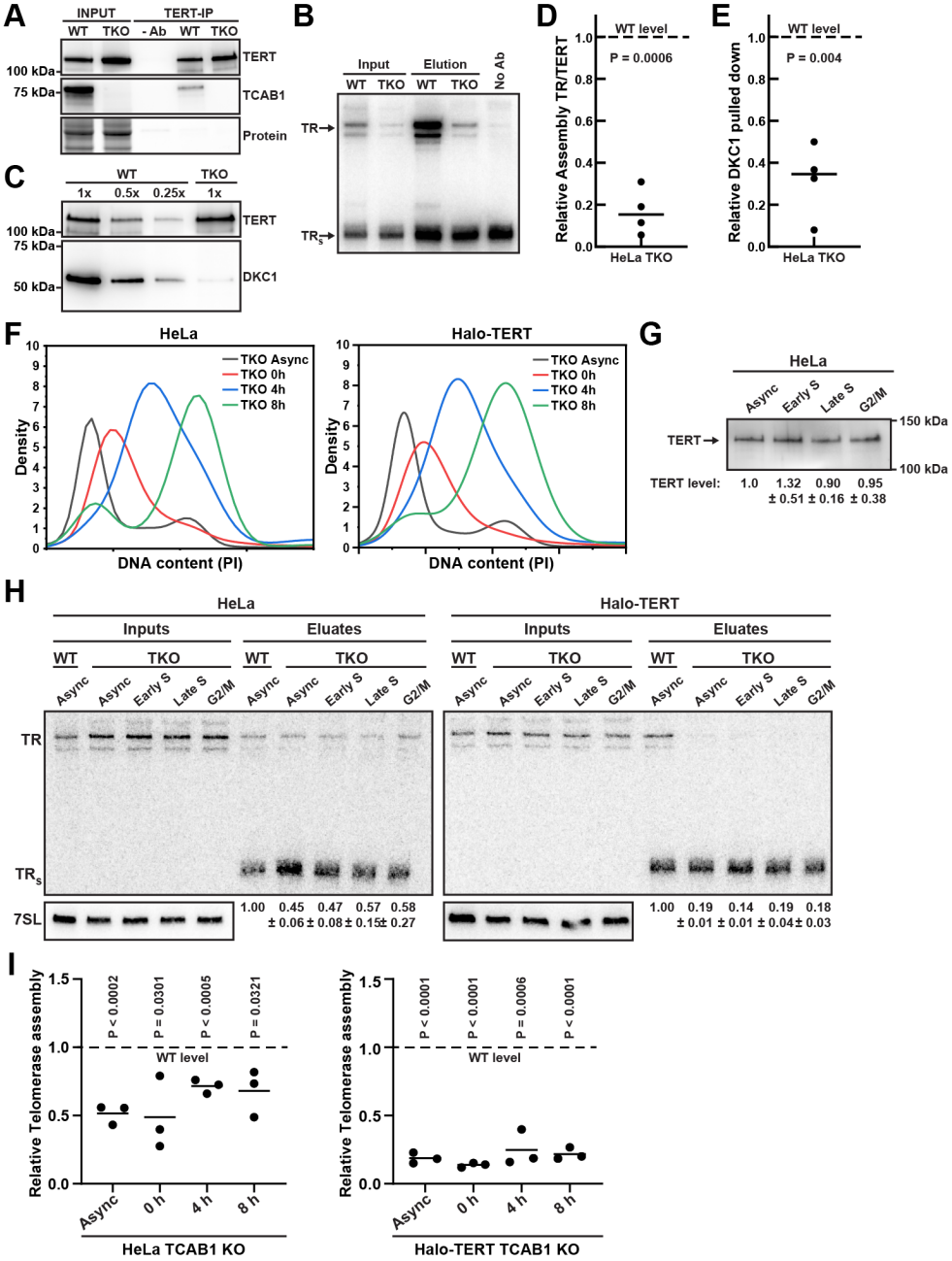

Supplementary Figure 2. (A) Western blots analyzing TERT immuno-purification (using a sheep anti-TERT antibody) from Halo-TERT cells overexpressing TERT and TR probed with a rabbit anti-TERT antibody (Abcam) and a TCAB1 antibody. **(B)** Northern blot of RNA extracted from input and purified TERT samples from Halo-TERT cells overexpressing TERT and TR probed with radiolabeled DNA oligonucleotides complementary to TR. Standards are *in vitro* transcribed full-length TR and truncated TR_S. TR_S was added to samples prior to RNA extraction as loading and recovery control. **(C)** Western blots to analyze immuno-purified telomerase RNP composition from Halo-TERT cells. A single membrane was cut into two pieces that were probed with TERT and dyskerin antibodies, respectively. **(D-E)** Quantification of the amount of **(D)** the ratio of TR to TERT (n = 4), and **(E)** dyskerin (n = 4) in TERT purifications from Halo-TERT TCAB1 knock-out cells overexpressing TERT and TR compared to parental controls (mean, T-Test). The dashed lines indicate the level in telomerase purified from wild-type TCAB1 control cells which was normalized to 1.0. **(F)** DNA content analysis (PI staining) by flow cytometry of synchronized cell populations

used for telomerase purifications. **(G)** Western blots analyzing endogenous TERT immuno-purifications (using a sheep anti-TERT antibody) from synchronized control HeLa and TCAB1 knock-out cells probed with a rabbit anti-TERT antibody (Abcam). **(H)** Northern blot of RNA extracted from input and purified TERT samples from asynchronous control HeLa cells and asynchronous and synchronized TCAB1 knock-out cells probed with radiolabeled DNA oligonucleotides complementary to TR. Standards are *in vitro* transcribed full-length TR and truncated TR_S. TR_S was added to samples prior to RNA extraction as loading and recovery control. Input samples were also probed for 7SL RNA as loading control. **(I)** Quantification of fraction of input TR (normalized to 7SL) co-purified with TERT or HaloTag-TERT (normalized to TR_s) from TCAB1 knock-out cells relative to control cells (dashed line).

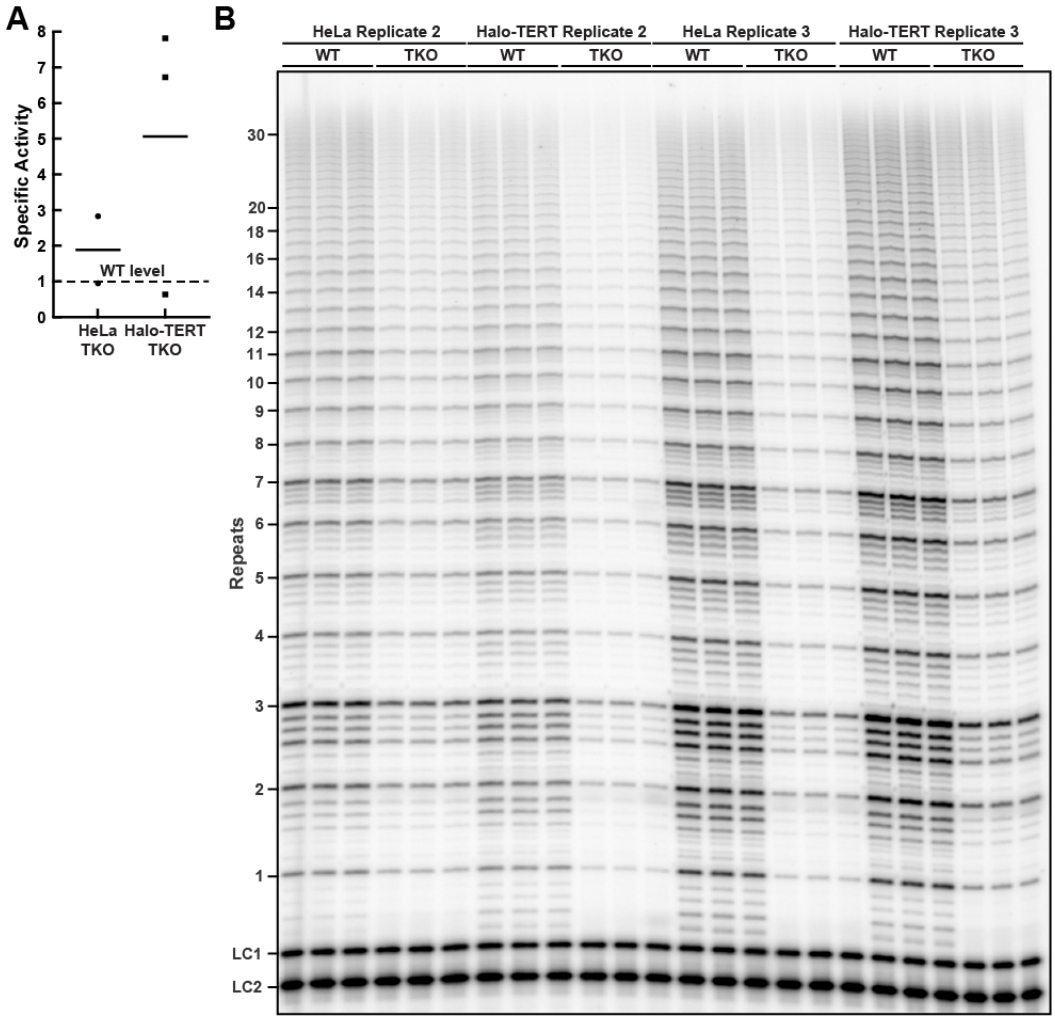

Supplementary Figure 3. (A) Specific activity of endogenous telomerase purified from TCAB1 knock-out cells relative to parental controls. Specific activity was calculated by dividing the relative activity (see Fig. 5A,B) by the relative amount of TR present in immuno-purified TERT samples (Fig. 4B). The dashed lines indicate the activity level in telomerase purified from wild-type TCAB1 control cells which was normalized to 1.0. **(B)** Direct telomerase extension assay of telomerase immuno-purified from parental (WT) and TCAB1 knock-out (TKO) HeLa and Halo-TERT cell lines. LC1 and LC2, radiolabeled DNA oligonucleotide loading controls.

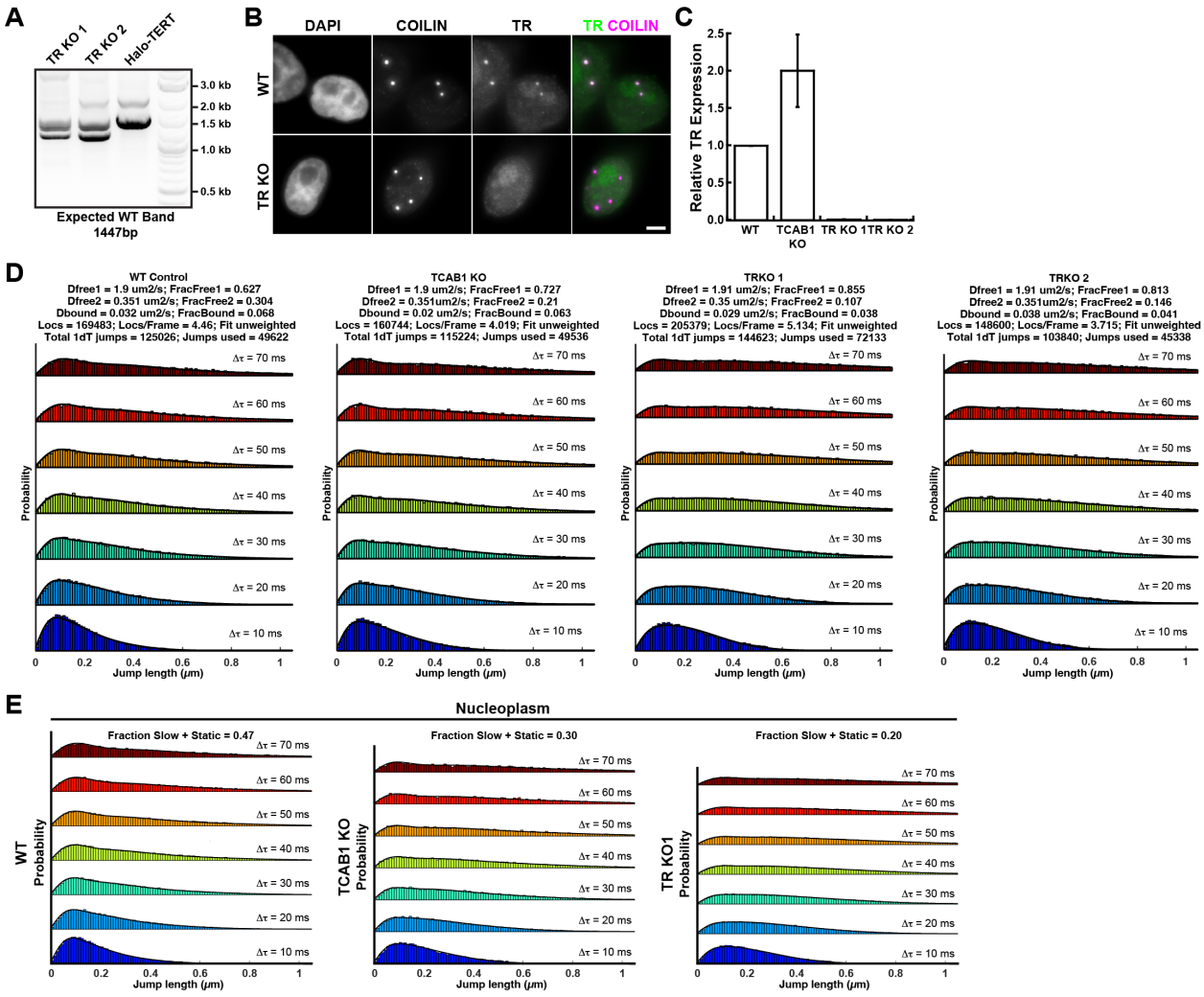

Supplementary Figure 4. (A) PCR analysis of the TR locus in parental and TR knock-out clones. Both TR knock-out clones show PCR products with reduced length that were confirmed to be knock-outs by Sanger sequencing. **(B)** Images of control and TR knock-out cells probed with an antibody against coilin and FISH probes specific for TR, demonstrating the lack of TR signal in TR knock-out cells (scale bar = 5 μm). **(C)** Determination of TR levels in control, TCAB1 knock-out, and TR knock-out cells, using RT-qPCR with primers specific to TR normalized to GAPDH (3 independent biological replicates, 3 technical replicates for each biological replicate, mean ± standard deviation). **(D)** Probability density function of step sizes of HaloTag-TERT molecules from control, TCAB1 knock-out, and TR knock-out cells and the corresponding 3-state model fit using the spot on tool (Data from one of three biological replicates, >15 cells per cell line). **(E)** Probability density functions of the step-sizes derived from nucleoplasmic HaloTag-TERT molecules and the corresponding 3-state model fit using the spot on tool (pooled data from 3 independent experiments, >18 cells total per cell line).

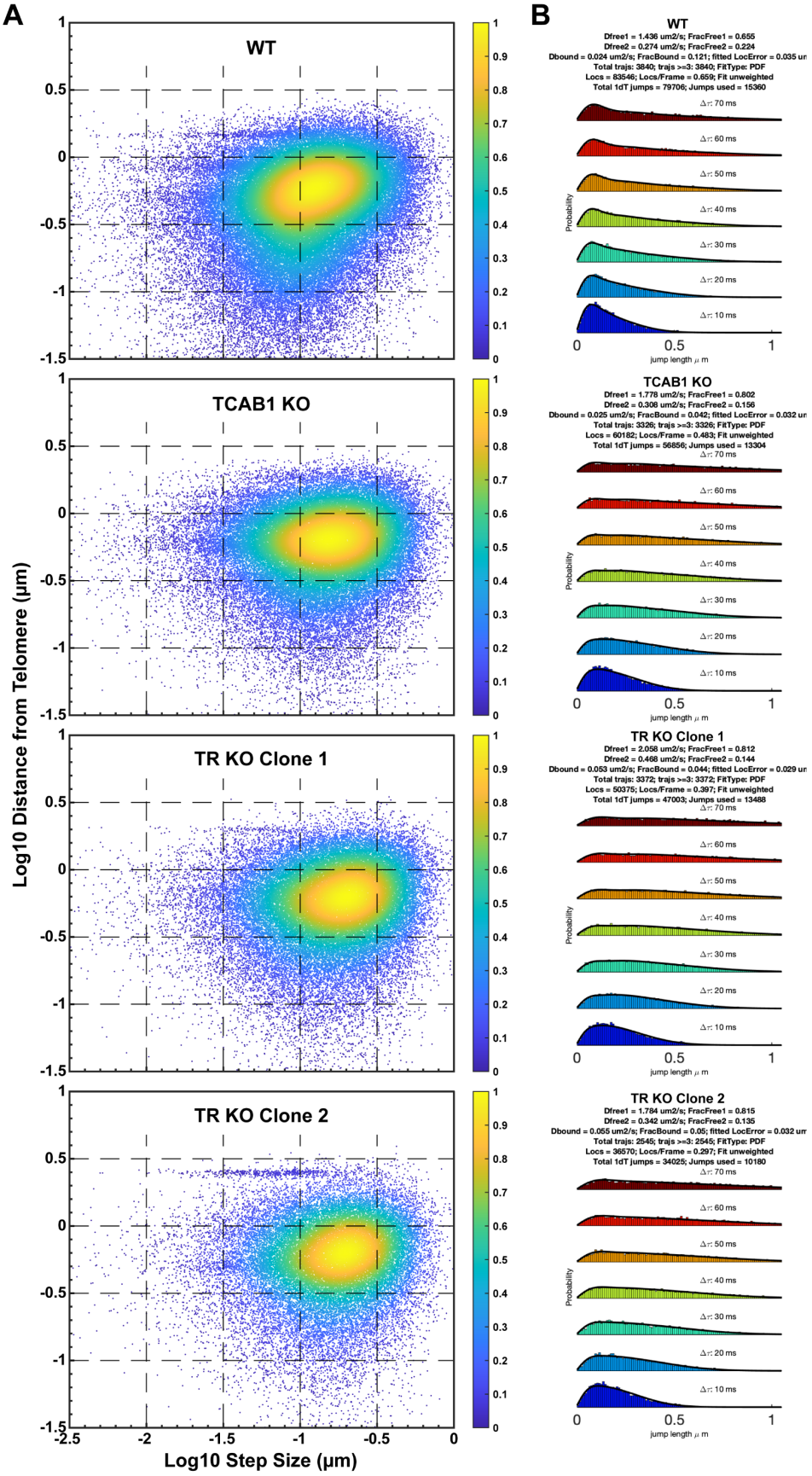
A
B
WT
TCAB1 KO
TR KO Clone 1
TR KO Clone 2
Log10 Distance from Telomere (μm)
Log10 Step Size (μm)
Dfree1 = 1.436 um2/s; FracFree1 = 0.655
Dfree2 = 0.274 um2/s; FracFree2 = 0.224
Dbound = 0.024 um2/s; FracBound = 0.121; fitted LocError = 0.035 ur
Total trajs: 3840; trajs >=3: 3840; FitType: PDF
Locs = 83546; Locs/Frame = 0.659; Fit unweighted
Total 1dT jumps = 79706; Jumps used = 15360
Dfree1 = 1.778 um2/s; FracFree1 = 0.802
Dfree2 = 0.308 um2/s; FracFree2 = 0.156
Dbound = 0.025 um2/s; FracBound = 0.042; fitted LocError = 0.032 ur
Total trajs: 3326; trajs >=3: 3326; FitType: PDF
Locs = 60182; Locs/Frame = 0.483; Fit unweighted
Total 1dT jumps = 56856; Jumps used = 13304
Dfree1 = 2.058 um2/s; FracFree1 = 0.812
Dfree2 = 0.468 um2/s; FracFree2 = 0.144
Dbound = 0.053 um2/s; FracBound = 0.044; fitted LocError = 0.029 ur
Total trajs: 3372; trajs >=3: 3372; FitType: PDF
Locs = 50375; Locs/Frame = 0.397; Fit unweighted
Total 1dT jumps = 47003; Jumps used = 13488
Dfree1 = 1.784 um2/s; FracFree1 = 0.815
Dfree2 = 0.342 um2/s; FracFree2 = 0.135
Dbound = 0.055 um2/s; FracBound = 0.05; fitted LocError = 0.032 ur
Total trajs: 2545; trajs >=3: 2545; FitType: PDF
Locs = 36570; Locs/Frame = 0.297; Fit unweighted
Total 1dT jumps = 34025; Jumps used = 10180
Δτ: 70 ms
Δτ: 60 ms
Δτ: 50 ms
Δτ: 40 ms
Δτ: 30 ms
Δτ: 20 ms
Δτ: 10 ms
Probability
jump length μ m

1221

Supplementary Figure 5. (A) Analysis if the step size of telomeric TERT particles relative to the distance of the particle to the closest telomere (pooled results from 3 independent biological replicates with 19-30 cells analyzed per replicate). TERT molecules bound to the telomere are expected to have small step sizes and a short distance to the closest telomere, which is apparent in the enrichment of events in the lower quadrants in the WT control. This enrichment is not observed in TCAB1 and TR knock-out cells. **(B)** Spot-On analysis of telomeric TERT particles (pooled results from 3 independent biological replicates with 19-30 cells analyzed per replicate). The fraction of bound TERT particles in TCAB1 and TR knock-out cells is 4-5%, compared to 12% in the WT control cells.

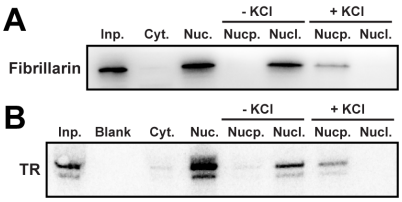

Supplementary Figure 6. (A) Western blot and **(B)** Northern blot of cellular fractions from TCAB1 knock-out cells probed with an antibody against fibrillarin and probes for TR, respectively. Ruptured nuclei were either maintained at a low salt concentration or exposed to 357.5 mM KCl. The results demonstrate that nucleoli are dissolved in the presence of a high salt concentration, releasing fibrillarin and TR into the nucleoplasmic fraction.

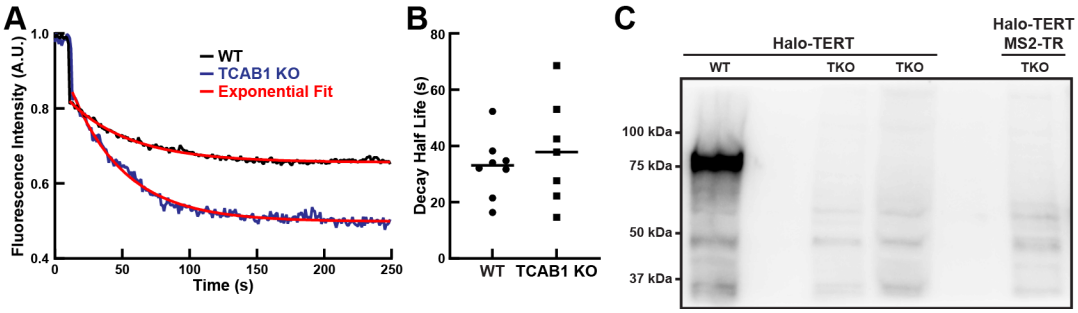

Supplementary Figure 7. (A) Fluorescence recovery curves of nucleolar dyskerin in the inbleached nucleolus of control and TCAB1 knock-out cells. Data was fit with a single exponential function. **(B)** Quantification of half-life of fluorescence recovery, calculated from the rate constant of the single exponential fit of the data shown in **(A)** (n = 8 and 7, mean). **(C)** Western blot probed with an antibody against TCAB1, demonstrating the knock-out of TCAB1 in Halo-TERT MS2-TR HeLa cells.

Movie Legends

Movie S1. Single-molecule imaging of 3xFLAG-HaloTag-TERT labeled with JFX650 and GFP-NPM1 to mark nucleoli in a control cell acquired at 100 frames per second second using an Andor iXon 897 Ultra camera. 200x200 pixels with a pixel size of 0.16 µm.

Movie S2. Single-molecule imaging of 3xFLAG-HaloTag-TERT labeled with JFX650 and GFP-NPM1 to mark nucleoli in a TCAB1 knock-out cell acquired at 100 frames per second second using an Andor iXon 897 Ultra camera. 200x200 pixels with a pixel size of 0.16 µm.

Movie S3. Movie of cell expressing GFP-nucleolin (red) and 3xFLAG-HaloTag-NLS (green) labeled with JF646 acquired at 100 frames per second using an Andor iXon 897 Ultra camera, showing overlap of 3xFLAG-HaloTag-NLS with nucleoli. 140x140 pixels with a pixel size of 0.16 µm.

Movie S4. Movie of 3xFLAG-HaloTag-TERT labeled with JF646 in a control (left), TCAB1 knock-out (middle), and TR knock-out (right) cell acquired at 100 frames per second using an Andor iXon 897 Ultra camera. Each panel is 150x150 pixels in size with a pixel size of 0.16 µm.

Movie S5. Single-particle tracking of 3xFLAG-HaloTag-TERT labeled with JF646 in a TR knock-out cells acquired at 100 frames per second using an Andor iXon 897 Ultra camera. Trajectories with a minimum of 5 localizations are displayed. 150x150 pixels with a pixel size of 0.16 µm.

Movie S6. Single-molecule imaging of 3xFLAG-HaloTag-TERT labeled with JFX650 and GFP-NPM1 to mark nucleoli in a control (left), TCAB1 knock-out (middle), and TR knock-out cells 6-hours after release from a double-thymidine block acquired at 100 frames per second using a Hamamatsu ORCA BT fusion camera. 220x220 pixels with a pixel size of 0.108 µm.

Movie S7. Single-molecule imaging of 3xFLAG-HaloTag-TCAB1 labeled with JFX650, GFP-NPM1 to mark nucleoli, and BFP-coilin to mark Cajal bodies acquired at 100 frames per second using an Andor iXon 897 Ultra camera. GFP-NPM1 and BFP-coilin signals were acquired before and after single-molecule imaging of 3xFLAG-HaloTag-TCAB1. 190x190 pixels with a pixel size of 0.16 µm.

Movie S8. Single-molecule imaging of 3xFLAG-HaloTag-TCAB1 labeled with JFX650 and GFP-NPM1 to mark nucleoli acquired at 100 frames per second using an Andor iXon 897 Ultra camera. GFP-NPM1 and BFP-coilin signals were acquired before and after single-molecule imaging of 3xFLAG-HaloTag-TCAB1. 190x190 pixels with a pixel size of 0.16 µm.

1299 **Movie S9.** Fluorescence recovery after photobleaching of HaloTag-dyskerin labeled with
1300 JFX650 HaloTag-ligand expressed in control cells acquired at 1 frame per second.
1301
1302 **Movie S10.** Fluorescence recovery after photobleaching of HaloTag-dyskerin labeled
1303 with JFX650 HaloTag-ligand expressed in TCAB1 knock-out cells, acquired at 1 frame
1304 per second.
1305
1306 **Movie S11.** Fluorescence recovery after photobleaching of nucleolar 3xMS2-TR bound
1307 by MCP-mNeonGreen, acquired at 1 frame per second using a Hamamatsu ORCA BT
1308 fusion camera. Nucleoli were identified by transient expression of mTagBFP-Nucleus-7.
1309
1310